On the impact of the turbulent grazing flow development on the acoustic response of an acoustic liner

Original
On the impact of the turbulent grazing flow development on the acoustic response of an acoustic liner / Paduano, A., Scarano, F., Cordioli, J., Casalino, D., Avallone, F.. - In: JOURNAL OF FLUID MECHANICS. - ISSN 0022-1120. - 1035:(2026). [10.1017/jfm.2026.11544]

Publisher:
Cambridge University Press

Published
DOI:10.1017/jfm.2026.11544

J. Fluid Mech. (2026), vol. 1035, A11, doi:10.1017/jfm.2026.11544

On the impact of the turbulent grazing flow development on the acoustic response of an acoustic liner

Angelo Paduano[1], **Francesco Scarano**[1], **Julio Cordioli**[2], **Damiano Casalino**[3] and **Francesco Avallone**[1]

[1]Department of Mechanical and Aerospace Engineering, Polytechnic of Turin, Turin, Italy

[2]Department of Mechanical Engineering, Federal University of Santa Catarina, Florianópolis, Brazil

[3]Flow Physics and Technology Department, Delft University of Technology, Delft, Netherlands

Corresponding author: Angelo Paduano, angelo.paduano@polito.it

(Received 29 July 2025; revised 19 January 2026; accepted 6 April 2026)

The interaction between acoustic waves and turbulent grazing flow over an acoustic liner is investigated using lattice-Boltzmann very-large-eddy simulations. A single-degree-of-freedom liner with 11 streamwise-aligned cavities is studied in a grazing flow impedance tube. The conditions replicate reference experiments from the Federal University of Santa Catarina. The influence of grazing flow (with a centreline Mach number of 0.32), acoustic wave amplitude, frequency and propagation direction relative to the mean flow is analysed. Impedance is computed using both direct (i.e. the *in situ* method) and model-fitting inference (i.e. the mode-matching) methods. The former reveals strong spatial variations; however, averaged values throughout the sample show minimal differences between upstream- and downstream-propagating waves, in contrast to what is obtained with the latter method. Flow analyses reveal that the orifices displace the flow away from the face sheet, with this effect amplified by acoustic waves and dependent on the wave propagation direction. Consequently, the boundary layer displacement thickness (δ^*) increases along the streamwise direction compared with a smooth wall and exhibits localised humps downstream of each orifice. The growth of δ^* alters the flow dynamics within the orifices by weakening the shear layer at downstream positions. This influences the acoustic-induced mass flow rate through the orifices at equal sound pressure level, suggesting that acoustic energy is dissipated differently along the liner. The asymmetry of the flow field experienced by the acoustic wave, depending on its propagation direction, highlights the need to consider a spatially evolving turbulent flow when studying the acoustic–flow interaction and measuring impedance.

Key words: aeroacoustics, turbulence simulation

---

1. Introduction

Acoustic liners are components of aircraft engines adopted to reduce noise (figure 1*a*). They are usually installed in the engines' intake and core jet section. The recent development of ultra-high bypass ratio engines, characterised by a larger fan diameter compared with traditional high-bypass ratio engines, has significantly increased the contribution of fan noise to the overall engine noise. This noise source consists of two main components: a tonal component at the blade-passing frequency (BPF) and its harmonics, and a broadband component generated by turbulence impingement of the fan wake on the stator, which arises from fan/stator proximity (Mallat 1989; Hughes 2011; Casalino, Hazir & Mann 2018).

Various classes of liners with customisable sound absorption properties exist, that range in complexity. Conventional acoustic liners consist of honeycomb cavities enclosed between a perforated face sheet and a rigid backplate (Motsinger & Kraft 1991), a configuration commonly referred to as a single-degree-of-freedom (SDOF) liner (figure 1*b*). They operate on the principle of a Helmholtz resonator to dissipate incident acoustic energy. The resonant frequency of the liner is typically tuned to coincide with the fan BPF or its harmonics, making SDOF liners particularly suitable for fan noise attenuation. The geometry of SDOF liners is defined by five key parameters: the number of orifices, their diameter d, the thickness τ of the facesheet and the cavity area A and depth ζ. In the absence of grazing flow, the resonant frequency is expressed as (Panton & Miller 1975)

$$f_0 = \frac{a_0}{2\pi}\sqrt{\frac{S}{V_c(\tau+\tau^*)+P}}, \tag{1.1}$$

where a_0 is the speed of sound, S is the orifice area and $V_c = A\zeta$ is the volume of the cavity. The terms $P = (1/3)\zeta^2 A$ and $\tau^* \approx 0.8\sqrt{S/\pi}$ are end corrections, accounting for the oscillatory motion of not only the fluid medium within the neck of the orifice but also a small portion of fluid inside the cavity and outside the orifice. In the realm of classical acoustics, SDOF liners are commonly regarded as locally reacting, meaning their response hinges solely on the local sound pressure level (SPL) and acoustic particle velocity rather than the angle of incidence of the acoustic wave (Motsinger & Kraft 1991; Rienstra & Hirschberg 2004). Essentially, this implies that the wavelength of the acoustic wave is significantly larger than the backing cavity width, thus no wave motion in the liner is possible in the transverse direction (Cummings 1976; Nilsson & Brander 1980).

A SDOF liner dissipates acoustic energy by viscosity at the orifice sidewalls and vortex shedding. The liner it is said to operate predominantly in the linear regime when the incident acoustic wave has a low SPL, conventionally below 130 dB (Scarano *et al.* 2025). In this case, the acoustic energy is mainly dissipated through viscous effects along the internal walls of the liner's orifices, where a laminar boundary layer develops (Tam & Kurbatskii 2000*b*). As the SPL increases, the dissipation mechanism is dominated by the formation of jets and vortex shedding at the mouths of the orifices (Howe 1984; Tam *et al.*

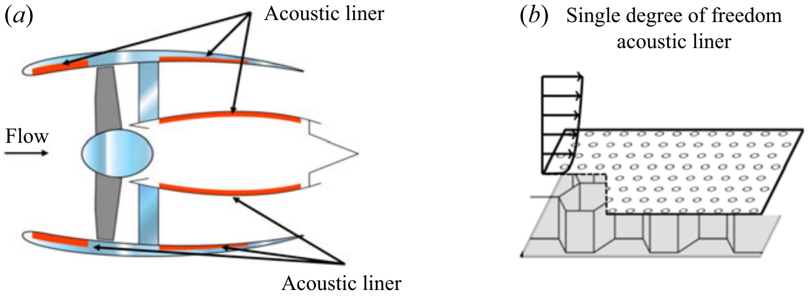

Figure 1. (*a*) Turbofan engine scheme with detail on location of acoustic liners, adapted from Sutliff (2021). (*b*) Sketch of a SDOF acoustic liner.

2010; Zhang & Bodony 2012; Léon *et al.* 2019). This regime is referred to as nonlinear. The acoustic energy is converted into turbulent kinetic energy, associated with the rotational motion of the vortices, which is subsequently dissipated as heat through viscous effects (Tam & Kurbatskii 2000*b*). According to Tam & Kurbatskii (2000*b*), vortex shedding is amplified at frequencies close to the liner's resonance, but it is not influenced by the angle of incidence of the acoustic waves. In a more recent experimental study, in the absence of flow, Tang, Wang & Liu (2024) showed the formation of multi-scale vortex structures excited by acoustic waves. Similar findings were also found numerically by Zhang & Bodony (2016) in the presence of grazing flow. They described how the flow field is linked to the acoustic response of an acoustic liner and how this changes if the boundary layer is laminar or turbulent. It was found that the impact of the boundary layer state (i.e. laminar or turbulent) is more pronounced at low SPL.

A widely used approach to characterise a liner is to utilise a spatially homogeneous quantity named acoustic impedance. It is defined in the frequency domain as

$$\hat{Z}(\omega) = \frac{\hat{p}}{\hat{\boldsymbol{v}} \boldsymbol{\cdot} \boldsymbol{n}} = \theta + i\chi, \tag{1.2}$$

where $\hat{p}$ is the acoustic complex pressure such that $p(\boldsymbol{x}, t) = \Re(\hat{p}\, e^{i\omega t})$, $\hat{\boldsymbol{v}} \boldsymbol{\cdot} \boldsymbol{n}$ is the acoustic particle velocity normal to the surface (with $\boldsymbol{n}$ denoting the unit normal vector pointing outward from the surface), with ω being the acoustic wave angular frequency. The quantity θ is the resistance and χ the reactance. Under this convention, $\chi > 0$ corresponds to mass-like behaviour, while negative reactance indicates spring-like behaviour (Rienstra & Hirschberg 2004). Although impedance is an intrinsic property of the liner's surface and shall remain independent of the duct geometry in which the liner is tested, several studies have highlighted its sensitivity to the eduction technique, i.e. the method used to calculate impedance (Avallone *et al.* 2024), and the flow profile within the duct (Quintino *et al.* 2025). The presence of a grazing flow introduces additional complexities to the impedance eduction process (Schulz *et al.* 2021) since impedance depends not only by geometrical and acoustic parameters like orifice diameter, face sheet thickness, cavity depth and SPL, but also by the flow Mach number and the boundary layer displacement thickness, δ^* (Nayfeh, Kaiser & Shaker 1974; Jones *et al.* 2002; Temiz *et al.* 2015; Bonomo *et al.* 2023; Quintino *et al.* 2025).

Even though the physics of acoustic liners is well known when they are exposed solely to an acoustic wave (Melling 1973; Tam & Kurbatskii 2000*a*), a gap persists in our knowledge when the liners operate in the presence of both an acoustic wave and grazing turbulent flow (Kooijman, Hirschberg & Golliard 2008; Murray & Astley 2012; Zhang & Bodony 2016; Avallone & Casalino 2021; Shahzad *et al.* 2023*b*). Hersh & Walker (1979) studied experimentally a multiple-orifice Helmholtz resonator with grazing flow. They found that the reactance depends on the orifice spacing, in particular when the orifices are aligned parallel to the grazing flow direction. The interaction between the acoustic-induced flow field and the grazing flow was visualised for the first time by Baumeister & Rice (1975). They identified the presence of a vortex at the upstream edge of the orifice neck, leading to a reduction in the effective inflow area. A more recent experimental study by Léon *et al.* (2019), using particle image velocimetry, showed how the near-orifice flow is altered in the presence of a grazing acoustic wave and turbulent flow. Their study highlighted the ratio between the acoustic velocity and the shear velocity as a key parameter governing the transition between linear and nonlinear operating regimes. These experiments provided valuable insights into the flow near the wall; however, the flow dynamics inside the orifice remains largely inaccessible to experimental observation and can only be comprehensively investigated through high-fidelity numerical simulations.

Several computational studies have investigated the physics of the flow within the orifice. Early efforts focused on simplified geometries in the absence of grazing flow (Tam & Kurbatskii 2000*a*), later progressing to cases incorporating grazing flow (Zhang & Bodony 2011; Avallone *et al.* 2019; Avallone & Casalino 2021). Fully three-dimensional numerical simulations of sound interacting with laminar and turbulent boundary layers were performed by Zhang & Bodony (2016). While these computational studies provide valuable descriptions of the flow and acoustic fields within the orifice, they remain confined to single-resonator configurations and do not account for boundary layer modifications induced by the presence of multiple cavities. In the recent study by Shahzad *et al.* (2023*b*), three-dimensional direct numerical simulations were conducted on channel flow with a full acoustic liner mounted on the walls. The work provided an in-depth characterisation of how the turbulent grazing flow is altered in the presence of the liner, with particular emphasis on the flow development within the orifices and the added aerodynamic drag. However, the absence of an acoustic source raises important questions regarding how incident acoustic waves modify the grazing flow and the flow topology within the orifices, and how these modifications influence the acoustic impedance. Tam *et al.* (2014) performed two-dimensional simulations of an array of eight-orifice slit resonators in the presence of acoustic waves. Particular attention was given to replicating the spatially developing flow in the Grazing Flow Impedance Tube at NASA Langley through a tuned eddy viscosity model along the duct. Despite the computed impedance showing similar trends as in the experiments, there were differences in the resistance and reactance values, especially at the lowest frequencies. In a more recent effort, Pereira *et al.* (2022) conducted lattice-Boltzmann very-large-eddy simulations (LB-VLES) of an array of eleven resonators, each composed of eight orifices. The computational set-up was designed to replicate the Federal University of Santa Catarina (UFSC) test rig. Different techniques were employed to educe impedance. Comparisons of impedance with experimental results revealed discrepancies up to a factor of two, highlighting that geometrical variations between the experimental sample and the one investigated numerically can affect the results (Bonomo *et al.* 2022; Paduano *et al.* 2024).

The utilisation of acoustic impedance to assess liner performance has spurred extensive investigation, leading to several semi-empirical models aimed at predicting this quantity. Hersh & Walker (1979) were among the first to devise a semi-empirical model to predict orifice resistance and reactance as a function of incident SPL, frequency and orifice geometry. Howe (1996) formulated an expression for the Rayleigh conductivity of an aperture subjected to a high-Reynolds-number flow, and Cummings (1987) established a connection between acoustic resistance and discharge coefficient via a quasi-steady model.

A semi-empirical model to account for linear and nonlinear effects was developed by Yu, Ruiz & Kwan (2008).

Studies have also shown that impedance can vary depending on the direction of acoustic wave propagation when a grazing flow is present (Renou & Aurégan 2011). This observation challenges the conventional assumption of locally reacting liners. Some of these impedance variations have been attributed to simplified approximations of the boundary layer within the Ingard–Myers boundary condition applied in impedance eduction techniques (Ingard 1959; Myers 1980). This boundary condition assumes an infinitely thin vortex sheet along the liner surface. Extensive research efforts aimed to incorporate boundary layer profiles with small but finite thicknesses into the impedance boundary conditions (Aurégan *et al.* 2001; Brambley 2011; Rienstra & Darau 2011). However, all these studies are based on the assumption of homogeneous liner impedance. In practice, liners consist of numerous small perforations and the significant variation that the boundary layer undergoes when interacting with the liner should be taken into account.

Based on the existing literature, it is a fact that the impact of the grazing flow development and its integral quantity must be accounted for. The literature still lacks a quantitative analysis of the acoustic and fluid dynamic fields over a multi-cavity acoustic liner when both the acoustic waves and the flow are grazing. This could provide the basis for developing robust semi-empirical models for impedance estimation and clarifying the role of acoustic wave direction in the presence of grazing flow. Furthermore, a clearer understanding of near-wall flow–acoustic interactions could help in the development of more effective acoustic liner geometries.

This study presents the results from high-fidelity numerical simulations conducted using LB-VLES on a nominal geometry that has been experimentally characterised (Quintino *et al.* 2025). The objective is to investigate the interaction between the acoustic field and the turbulent boundary layer, with a particular focus on the near-wall flow and in-orifice dynamics that influence the liner's acoustic response. To explore these effects, a wide range of acoustic waves, varying in amplitude, frequency and propagation direction, have been simulated. As a result, a comprehensive and open-access database has been developed, which is a valuable benchmark for future studies on acoustic–flow interactions over acoustic liners.

The paper is organised as follows: § 2 summarises the methodology and the post-processing techniques, § 3 describes the computational set-up and the grid convergence study, § 4 discusses the acoustic results, § 5 discusses fluid dynamic findings, § 6 delves into acoustic-induced flow within the orifices and § 7 draws main conclusions.

2. Methodology

2.1. *Flow solver*

The commercial software 3DS Simulia PowerFLOW© version 6 has been used. The solver is based on the lattice-Boltzmann method (LBM). A comprehensive introduction to the method can be found in Succi (2001). In the LBM framework, the fluid is described at a mesoscopic level through particle distribution functions, whose statistical moments yield the macroscopic quantities such as density, momentum and energy.

The method originates from the continuous Boltzmann equation, which reads

$$\frac{\partial \boldsymbol{g}}{\partial t} + \boldsymbol{\xi} \cdot \frac{\partial \boldsymbol{g}}{\partial \boldsymbol{x}} + \boldsymbol{F} \cdot \frac{\partial \boldsymbol{g}}{\partial \boldsymbol{\xi}} = \varOmega(g), \tag{2.1}$$

where $\boldsymbol{g}(\boldsymbol{\xi}, \boldsymbol{x}, t)$ is the particle distribution function, giving the mass density of particles located within the mesoscopic volume $\mathrm{d}\boldsymbol{x}$ around $\boldsymbol{x}$ and in the infinitesimal time interval

$(t, t + \mathrm{d}t)$ having a microscopic velocity within $(\boldsymbol{\xi}, \boldsymbol{\xi} + \mathrm{d}\boldsymbol{\xi})$. The left-hand side represents free streaming and the effect of external forces $\boldsymbol{F}$ and $\varOmega(g)$ is the collision operator and describes the interaction between particles. The Bhatnagar–Gross–Krook model (Bhatnagar, Gross & Krook 1954) is adopted thanks to its simplicity

$$\varOmega(g) = -\frac{1}{\tau}(g - g^{eq}), \tag{2.2}$$

where τ is the relaxation time and g^{eq} is the equilibrium distribution function derived from the Maxwell–Boltzmann equilibrium distribution. In the LBM formulation, the continuous distribution function is discretised in velocity space, yielding a finite set of discrete distributions $\boldsymbol{g_i}$ associated with discrete velocities $\boldsymbol{\xi_i}$. The particle transport and collisions are solved on a Cartesian mesh (lattice); the discrete volume elements are called voxels (vx). The D3Q19 lattice scheme is employed, where 'D3' refers to three spatial dimensions and 'Q19' to the number of discrete velocity directions (Qian, D'Humières & Lallemand 1992).

Hence, the macroscopic flow quantities density ρ and velocity $\boldsymbol{u}$ are obtained by discrete integration

$$\rho(\boldsymbol{x}, t) = \sum_i \boldsymbol{g_i}(\boldsymbol{x}, t), \quad \rho\boldsymbol{u}(\boldsymbol{x}, t) = \sum_i \boldsymbol{\xi_i}\boldsymbol{g_i}(\boldsymbol{x}, t). \tag{2.3}$$

A VLES approach has been employed to resolve only the larger turbulence scales. The sub-grid scales are accounted for by adding a turbulent relaxation time to the viscous relaxation time using a turbulence model, based on the two-equation renormalisation group theory (RNG) $k - \epsilon$, where k is the turbulent kinetic energy and ϵ is its dissipation rate, (Yakhot & Orszag 1986) given by

$$\tau_{eff} = \tau + C_\mu \frac{k^2/\epsilon}{(1 + \eta^2)^{1/2}}, \tag{2.4}$$

where $C_\mu = 0.09$ and η is a combination of the local strain, local vorticity and local helicity parameters. The term η allows for mitigation of the sub-grid-scale viscosity, in the presence of large resolved vortical structures (Texeira 1998).

It should be pointed out that the usage of the $k - \epsilon$ RNG model under the LBM-VLES framework differs significantly from its application in Reynolds-averaged Navier–Stokes (RANS) simulations. In RANS, the Reynolds stress tensor is computed directly using the turbulence model to solve a closure problem. In contrast, under the LBM-VLES framework, the turbulence model modifies the relaxation properties of the Boltzmann equation, thereby influencing the local eddy viscosity. The Reynolds stresses are a consequence of the computed turbulent chaotic motion and not a model add-on to the governing flow equations. This implementation enables the development of large turbulent eddies in the simulation domain and recovers to some extent a nonlinear constitutive form of the Reynolds stresses.

The solver uses an extended turbulent wall model that dynamically incorporates the presence of a pressure-gradient-extended wall-model (Texeira 1998). This model takes into account the effect of the pressure gradient by rescaling the length scale y^+, in the generalised law-of-the-wall (Launder & Spalding 1974), by a scaling parameter A

$$u^+ = \frac{1}{k} ln\left(\frac{y^+}{A}\right) + B, \tag{2.5}$$

where B and k are constants, $y^+ = (u_\tau y)/\nu$ and A is a function of the pressure gradient. The parameter A captures the physical consequence of the velocity profile slowing down

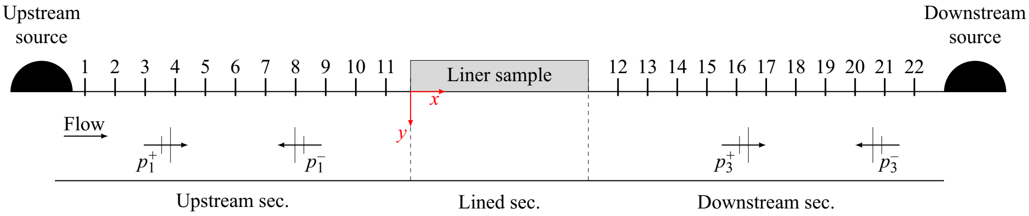

Figure 2. Representation of the acoustic field in the MM method and schematic view of the test rig.

and expanding due to the pressure gradient. It is defined as proposed by Texeira (1998)

$$A = 1 + \frac{\beta \left| \dfrac{\mathrm{d}p}{\mathrm{d}s} \right|}{\tau_w}, \quad \boldsymbol{u} \cdot \frac{\mathrm{d}p}{\mathrm{d}s} > 0, \tag{2.6}$$

$$A = 1, \quad \text{otherwise}; \tag{2.7}$$

where τ_w is the wall shear stress, $\mathrm{d}p/\mathrm{d}s$ is the streamwise pressure gradient, $\boldsymbol{u}$ is the streamwise velocity and β is a length of the same order as the unresolved near-wall region.

2.2. *Impedance measurement techniques*

Two techniques have been used to compute impedance: the mode-matching (MM) (Elnady & Bodén 2004) and the *in situ* (Dean 1974) methods.

2.2.1. *Mode matching method*

The MM method is an inverse impedance eduction method. It is based on minimising the difference between a computed acoustic field and measurements by iteratively varying the liner impedance. This method was first proposed by Elnady & Bodén (2004) and subsequently validated by Elnady, Bodén & Elhadidi (2009).

This method requires pressure measurements upstream and downstream of the liner. Figure 2 shows a schematic representation of probes location inside the duct. The measured acoustic pressure at the rigid wall, opposite the lined one, can be written as

$$p(x, y, z) = \sum_{q=1}^{Q} A_q^+ \, \Phi_q^+(y, z) \, \mathrm{e}^{-ik_{xq}^+ x} + \sum_{q=1}^{Q} A_q^- \, \Phi_q^-(y, z) \, \mathrm{e}^{-ik_{xq}^- x}, \tag{2.8}$$

where superscripts + and − denote incident and reflected waves propagating in the positive and negative x-directions, q is the modal index, $A_q^{\pm}$ are the modal amplitudes, k_{xq} is the axial wavenumber of mode q, obtained from the dispersion relation, and Φ is the mode shape. The method assumes that only plane waves propagate in the hard-wall sections, which is justified since the channel has an infinite width and the frequencies considered are below the first cut-on frequency. Under this assumption, p_1^+ represents the plane wave excited by the active source, p_3^- is the reflected plane wave at the duct termination and p_1^- and p_3^+ represent the scattered plane waves at the liner edges.

Since the set-up employs acoustic sponge layers, no acoustic waves are reflected at the duct termination. Therefore, $p_3^- = 0$ when the acoustic source is located upstream, and $p_1^+ = 0$ when it is located downstream. Viscothermal losses are accounted for by correcting the plane wave axial wavenumber

$$k_{x1}^{\pm} = \frac{\pm \omega K_0}{(1 \pm K_0 M)}, \tag{2.9}$$

where K_0 is the first-order Kirchhoff solution given by

$$K_0 = 1 + \frac{1-i}{Sh\sqrt{2}}\left(1 + \frac{\gamma - 1}{\sqrt{Pr}}\right), \tag{2.10}$$

and $Sh = r\sqrt{\omega/\nu}$ is the shear wavenumber, r is the hydraulic radius, $\gamma = 1.4$ is the heat capacity ratio and $Pr = 0.7$ is the Prandtl number. By using eleven microphones in each section, an over-determined system is obtained. Solving this system of equations in a least-squares sense for each set of microphones gives the amplitude of the waves propagating forward and backwards in the channel; these are used as inputs for the MM model. An initial guess on impedance for the lined section is obtained using the semi-empirical model by Yu *et al.* (2008). Then the impedance is obtained by minimising a cost function using the Levenberg–Marquardt algorithm (Levenberg 1944; Marquardt 1963). The cost function is defined as

$$F(Z) = \sum_{i=1}^{22} \left| \frac{p_i^{meas} - p_i^{analytic}(Z)}{p_i^{meas}} \right|. \tag{2.11}$$

Once the convergence criterion is satisfied, the liner impedance is obtained.

2.2.2. *In situ technique*

The *in situ* technique, also known as the two-microphones method, was first proposed by Dean (1974). It requires unsteady pressure measurements at the face sheet and the bottom of the cavity. This method provides a point-wise measurement of impedance. It is based on the following key assumptions: the wavelength of the incident acoustic wave is significantly larger than the cavity width. The walls of the cavity are considered to be sufficiently thick, resulting in the liner being locally reactive; any wave entering the cavity is assumed to be reflected at the backplate. Therefore, the acoustic pressure of the standing wave within the cavity is the sum of the incident and reflected ones. Using the linearised momentum equation, it is possible to calculate the acoustic-induced velocity and, subsequently, the impedance as

$$Z_f = \frac{Z}{Z_0} = -i\tilde{H}_{fb}\frac{1}{\sin(k\zeta)}, \tag{2.12}$$

where Z_0 is the characteristic impedance of air, $\tilde{H}_{fb}$ is the transfer function defined as the ratio between the pressure measured at the face sheet $\tilde{p}_f$ and at the backplate $\tilde{p}_b$, ζ is the depth of the cavity and $k = \omega/c_0$ is the free-field wavenumber. This technique has been widely used for estimating the impedance of acoustic liners in the presence of grazing flow (Schuster 2012; Zhang & Bodony 2016). Unlike impedance eduction techniques, this approach does not require a flow-based boundary condition for capturing near-wall acoustic–flow interactions. However, studies have underlined the sensitivity of this technique to the sampling position (Avallone & Casalino 2021).

To ensure a robust comparison with experimental data, impedance values from the *in situ* method have been sampled at the same locations as in the experiments. Figure 3(*b*) presents a schematic representation of the *in situ* sampling position. Additionally, since simulations provide access to the pressure values over the entire liner surface, the minimum, maximum and mean values across the cavities have also been extracted and analysed.

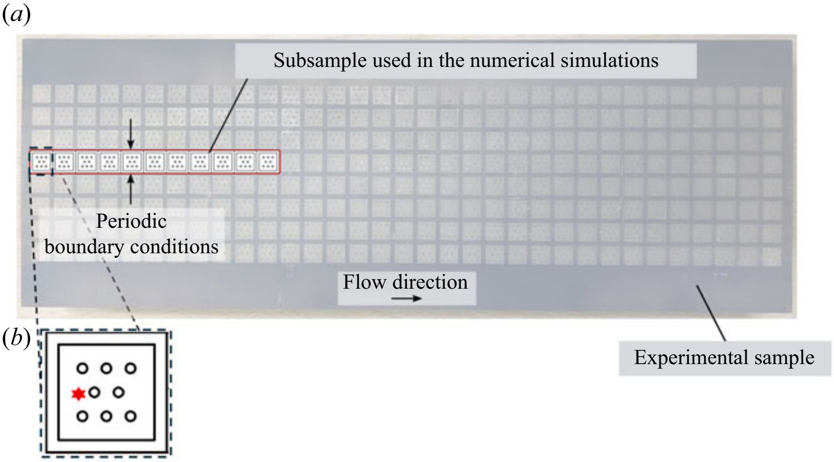

Figure 3. (*a*) Comparison between the real UFSC sample and the modelled geometry for the simulations. (*b*) Detail of the sampling location for the *in situ* technique for both experiments and simulations. ✸ Denotes the face sheet probe.

2.3. *Triple decomposition*

To describe the influence of the grazing flow on the in-orifice flow dynamics, examining the acoustic-induced velocity profiles is crucial. Extracting this information requires isolating the coherent acoustic-induced velocity field from the stochastic turbulent fluctuations. The triple decomposition method is employed to separate these contributions (Avallone & Casalino 2021).

The method consists of the following steps: the time series extracted from the LB-VLES simulations are initially phase locked with the incoming acoustic wave; the resultant phase-locked velocity components are denoted as $\tilde{u}$, $\tilde{v}$, $\tilde{w}$. These phase-locked fields are then averaged, yielding the corresponding mean velocity components, indicated as U, V, W. The acoustic-induced velocity components are subsequently determined by subtracting the phase-averaged fields from the phase-locked fields, yielding $\tilde{\tilde{u}}$, $\tilde{\tilde{v}}$, $\tilde{\tilde{w}}$. This method provides a straightforward approach for separating the acoustic-induced and the turbulent flow fields. Although it is not effective when the acoustic excitation involves broadband or non-tonal signals, because it is not possible to phase lock the signals, the present study considers only tonal plane waves, making this approach well suited.

3. Computational set-up

3.1. *Computational domain*

The computational domain is illustrated in figure 4. The coordinate system is defined as follows: x denotes the streamwise direction, y the wall-normal direction and z the spanwise direction. In this work, the following velocity notation is used: U, V, W: time-averaged streamwise, wall-normal and spanwise velocity components, respectively; u, v, w: instantaneous streamwise, wall-normal and spanwise velocity components; $u' = u - U,\ v' = v - V,\ w' = w - W$: velocity fluctuations relative to the mean.

The liner is placed in the middle of the channel at the top wall of a duct with a rectangular cross-section. Each cavity has a square cross-section of $l = 8.46d$ and a depth of $\zeta = 32.56d$, where $d = 1.17$ mm is the orifice diameter. Each cavity has eight orifices,

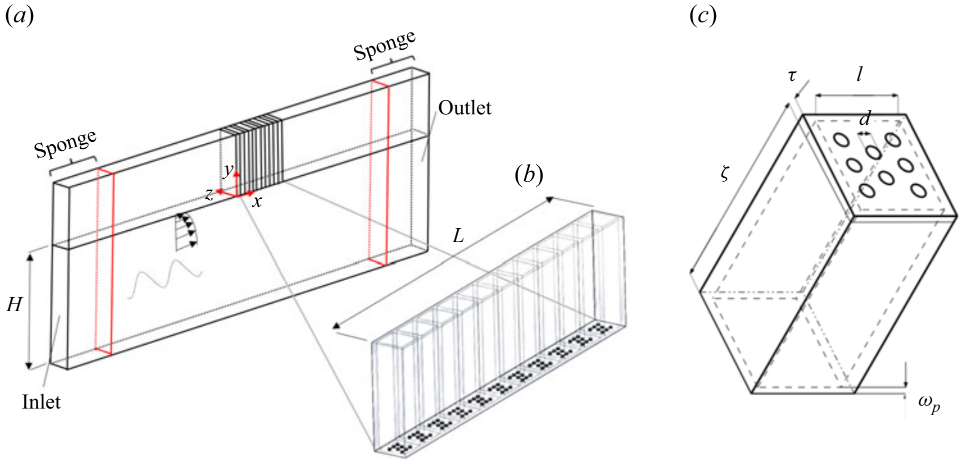

Figure 4. Schematic representation of the full computational domain.

partition walls of thickness $w_p = 1.08d$ and a face sheet thickness of $\tau = 0.46d$. These dimensions result in a percentage of open area for the entire sample of 5.5 %. The cross-section of the channel has a height of $H = 2h = 40$ mm and a width equal to $l + w_p$. In the upstream region of the channel, a zig-zag trip was added on both the top and bottom walls. Its size and position were manually adjusted to match the experimental velocity profile upstream of the liner. The zig-zag trip was placed at $x = -1367d$ upstream of the liner, where $x = 0$ marks the start of the liner. The zig-zag trip had a height of $0.21d$ and a length of $1.71d$.

To achieve a quasi-anechoic condition and prevent acoustic reflections at the channel's termination, the fluid viscosity was significantly increased using sponge regions, as shown in figure 4. In these regions, the viscosity was increased by a factor of one hundred following an exponential law. All walls in the computational domain were treated as adiabatic. A uniform velocity boundary condition was applied at the inlet, corresponding to a Mach number of $M = 0.3$, which results in a centreline velocity of $U_0 = 110\,\mathrm{m\,s^{-1}}$ ($M = 0.32$) in the lined section. A pressure boundary condition was set at the outlet.

The computational domain was designed to replicate the experimental set-up of the UFSC Liner Test Rig (Bonomo *et al.* 2022). The design of the sample, although resembling the one presented in a previous numerical study (Pereira *et al.* 2023), exhibits variations in terms of the face sheet thickness, orifice diameter and shape of the edges of the orifice, which were slightly rounded as discovered from the three-dimensional scanning of the tested liner sample (Quintino *et al.* 2025). Due to manufacturing limitations, the scan also identified variability in these parameters along the sample. Therefore, averaged values of orifice diameter and face sheet thickness were used to construct the liner sample for the numerical simulations. However, a few differences between the real and simulated liners should be noted. First, the simulated liner is represented by a single row of eleven cavities, while the one tested in the experiments features an 8 × 33 cavity grid, as shown in figure 3. However, both configurations maintain the same number of orifices per cavity, ensuring consistency in porosity. A second key difference is that, in the UFSC Liner Test Rig, the duct has a rectangular cross-section of $100 \times 40\,\mathrm{mm^2}$. In contrast, the simulation assumes periodic boundary conditions on both sides of the duct. Previous studies (Tam *et al.* 2014) have shown that this choice has minimal influence on the acoustic response, supporting the validity of the comparison with the experimental results.

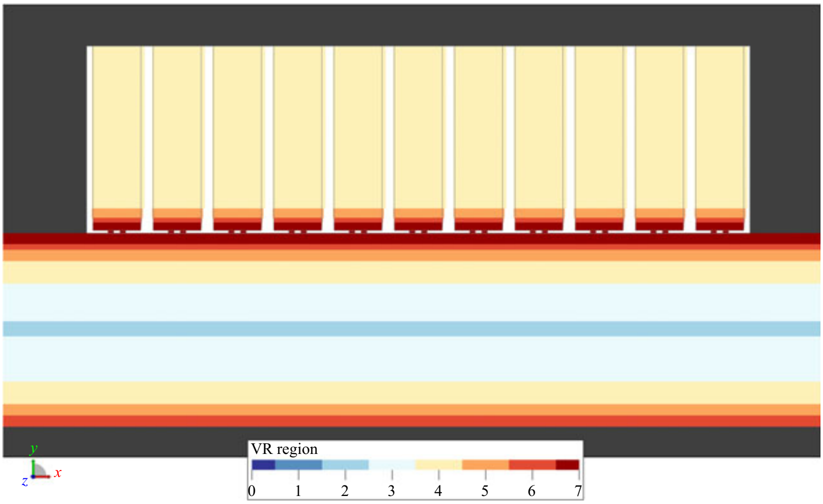

Figure 5. Schematic representation of the VR regions.

3.2. *Computational grid design*

A variable resolution (VR) scheme was adopted. Details of the VR regions are provided in figure 5. The VR regions are symmetric with respect to the centre of the channel. The finest resolution, VR = 7, was used to discretise the entire face sheet, the orifices and portions of the backing cavities. Each subsequent resolution level was defined by doubling the cell size of the previous level. Within the orifice, the minimum grid spacing was $\Delta z_{min} = \Delta y_{min} = \Delta x_{min} = 0.0207d$, yielding a resolution of ≈ 48 vx/d for the fine mesh. This results in a spacing expressed in wall units equal to $\Delta x^+ = \Delta y^+ = \Delta z^+ = 6.9$. Where $\Delta x^+ = \Delta x u_\tau / \nu$ and $u_\tau = \sqrt{\tau_w/\rho} = 4.2\,\mathrm{m\,s^{-1}}$ refers to the friction velocity of the smooth reference surface.

3.3. *Simulation strategy and test cases*

In the presence of the grazing flow, the flow developed spatially in the channel flow until statistical convergence was achieved. After achieving statistical convergence, the acoustic simulations were performed. Starting from the flow-only converged solution, an instantaneous flow field was saved and modified by superimposing a plane acoustic wave with a specified frequency and amplitude using the OptydB toolkit. This modified flow field was used as the initial condition for the subsequent simulations, which include the acoustic wave (Avallone *et al.* 2019).

While this approach effectively reduced computational costs, especially when analysing multiple configurations, it introduced a change in the initial condition that required a few acoustic cycles for the solution to reach a statistically steady state. For each configuration, the plane acoustic wave was at least 10 wavelengths long. The downside of this approach is that the length of the channel must be long enough to accommodate 10 acoustic wave wavelengths for the lowest frequency of interest. However, this approach is also beneficial since it allows the presence of acoustic sponges, thus minimising the impact of acoustic reflections at the boundary of the computational domain. Details on the computational cost are reported in Appendix A.2.

Twenty different simulations were performed and grouped into seven sets, as shown in table 1. Sets (A) and (B) consist of simulations with the acoustic liner, without grazing

Mach	Configuration	Acoustic source Pos.	Amplitude (dB)	Frequency (Hz)
		Set (A)		
0.00	Lined	Upstream	130	800
0.00	Lined	Upstream	130	1400
0.00	Lined	Upstream	130	2000
		Set (B)		
0.00	Lined	Upstream	145	800
0.00	Lined	Upstream	145	1400
0.00	Lined	Upstream	145	2000
		Set (C)		
0.32	Smooth	—	—	—
0.32	Lined	—	—	—
		Set (D)		
0.32	Lined	Upstream	130	800
0.32	Lined	Upstream	130	1400
0.32	Lined	Upstream	130	2000
		Set (E)		
0.32	Lined	Upstream	145	800
0.32	Lined	Upstream	145	1400
0.32	Lined	Upstream	145	2000
		Set (F)		
0.32	Lined	Downstream	130	800
0.32	Lined	Downstream	130	1400
0.32	Lined	Downstream	130	2000
		Set (G)		
0.32	Lined	Downstream	145	800
0.32	Lined	Downstream	145	1400
0.32	Lined	Downstream	145	2000

Table 1. List of the simulations carried out.

flow and with plane acoustic waves with amplitudes equal to 130 and 145 dB, and three frequencies (800, 1400 and 2000 Hz). The acoustic wave was located upstream of the liner. These frequencies were chosen to investigate the acoustic liner's behaviour near the resonance frequency and at frequencies above and below it. The SPL was calculated using the standard reference pressure of 20×10^{-6} Pa.

For the cases with grazing flow, the centreline Mach number was set to 0.32, as in the reference experiments. This corresponds to a bulk Reynolds number of $Re_b = 2.7 \times 10^5$ and a friction Reynolds number of $Re_\tau \approx 3500$. Set (C) includes two simulations: one of a turbulent channel flow with smooth walls and the other of a turbulent channel flow with the liner mounted in the upper wall. All other sets account for the presence of grazing turbulent flow and acoustic waves. Set (D) contains simulations with different frequencies, at an SPL of 130 dB and an upstream-located acoustic source, i.e. propagating in the same direction as the mean flow. Set (E) includes simulations with different frequencies at a fixed SPL of 145 dB and an upstream acoustic source. Sets (F) and (G) include simulations with different frequencies, and downstream acoustic sources at an SPL of 130 and 145 dB, respectively.

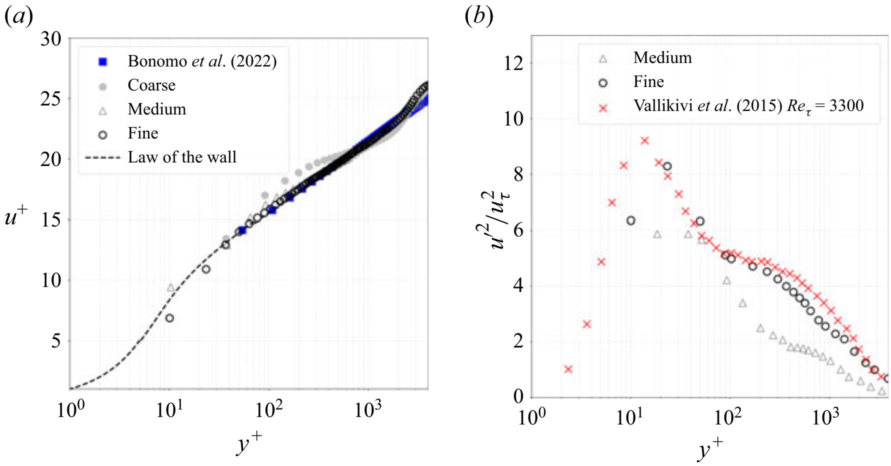

Figure 6. (*a*) Mean velocity profile comparison with experimental data by Bonomo *et al.* (2022); (*b*) streamwise velocity variance compared with experiments by Vallikivi *et al.* (2015).

3.4. *Validation of the numerical approach*

To validate the computational results, first the mean flow profile for the smooth-wall configuration was compared with the experimental data from Vallikivi, Hultmark & Smits (2015) and Bonomo *et al.* (2022) using three different mesh resolutions: coarse (12 vx/d), medium (24 vx/d) and fine (48 vx/d). Literature data were also used because velocity fluctuation measurements were not available from the experiments conducted by Bonomo *et al.* (2022).

Data are presented in wall units ($y^+ = yu_\tau/\nu$ and $u^+ = U/u_\tau$). In the experiments, the friction velocity was computed using the Clauser chart technique (Clauser 1954). In the simulations, u_τ was computed from the wall shear stress calculated using the extended wall model described in § 2. Figure 6(*a*) shows the mean velocity profile. The data from experiments by Bonomo *et al.* (2022) and simulations at the three resolutions are compared with the law-of-the-wall using constants $k = 0.37$ and $B = 3.7$, as recommended for turbulent channel flows (Nagib & Chauhan 2008). A good agreement between experiments and simulations is found.

Figure 6(*b*) presents measurements of the streamwise Reynolds stress derived from simulations, compared with experimental data reported by Vallikivi *et al.* (2015) at a friction Reynolds number of $Re_\tau \approx 3300$. Values were made non-dimensional using the local u_τ^2. The profile of u'^2 for the fine simulation is similar to the experiments at a comparable Reynolds number. Further validation of the simulation was performed by comparing the friction coefficient C_f, computed from the streamwise pressure drop, against the experimental data of Schultz & Flack (2013). The comparison, presented in Appendix A, confirms the reliability of the numerical predictions.

Based on these results, the fine-resolution grid was selected for all subsequent analyses.

4. Acoustic field and impedance distribution

Before analysing the flow field and examining how the acoustic liner and acoustic waves influence the streamwise evolution of the flow within the channel, we first describe the SPL distribution along the liner and the impedance values.

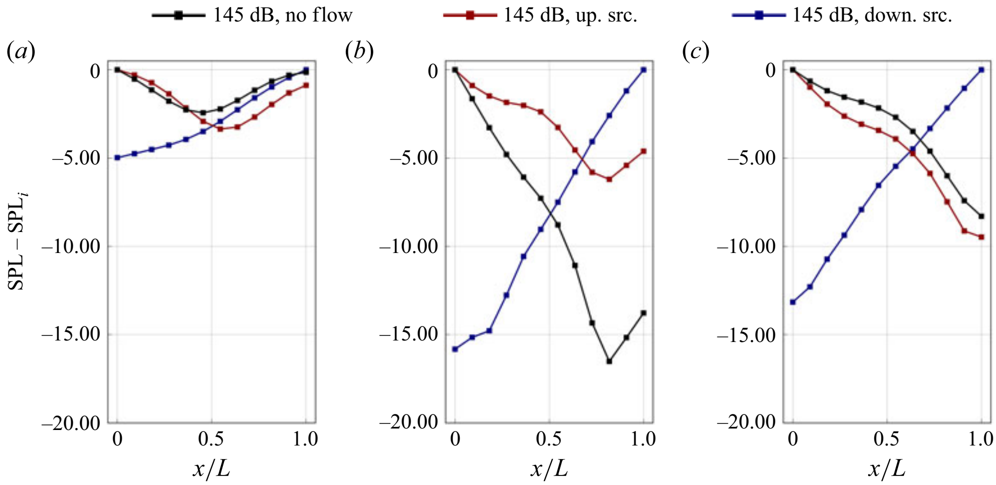

Figure 7. Sound pressure level decay along the channel centreline ($y/h = -1$) for an incident acoustic wave with SPL = 145 dB under different flow conditions: (*a*) $f = 800$ Hz, (*b*) $f = 1400$ Hz and (*c*) $f = 2000$ Hz. The SPL is normalised with respect to the incident SPL (SPL$_i$). The label 'src.' denotes the acoustic source location.

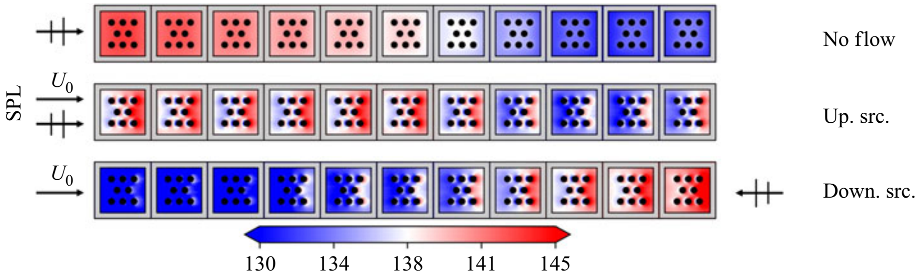

Figure 8. Sound pressure level along the liner's surface for the case with SPL = 145 dB and $f = 1400$ Hz under three conditions: without grazing flow, with grazing flow and upstream acoustic source and with grazing flow and downstream acoustic source.

4.1. *Sound pressure level decay*

The analysis starts with the SPL distributions at the centreline of the channel (figure 7), where the acoustic pressure fluctuations are almost not affected by the flow-induced ones. The SPL distribution is plotted with respect to the incident SPL$_i$ for each case. Although the SPLs were set equal for both simulations, minor deviations of approximately 2 dB (≈ 50 Pa) at the onset of the liner are present, which might be caused by different reflections of the acoustic waves at the wall impedance discontinuity depending on the propagation direction in the presence of flow (Saverna, Aurégan & Pagneux 2019). The shape of the SPL curves depends on the presence of grazing flow, the direction of acoustic wave propagation and its frequency. A relevant observation is that the SPL decays more when the source is located downstream, i.e. propagates against the mean flow, independently of the frequency of the acoustic wave. Furthermore, in this case, the SPL curves show a more monotonic behaviour compared with cases where the acoustic wave propagates in the same direction as the mean flow.

Figure 8 shows the distribution of SPL on the liner surface for the cases with an incoming acoustic plane acoustic wave with a frequency of 1400 Hz and SPL of

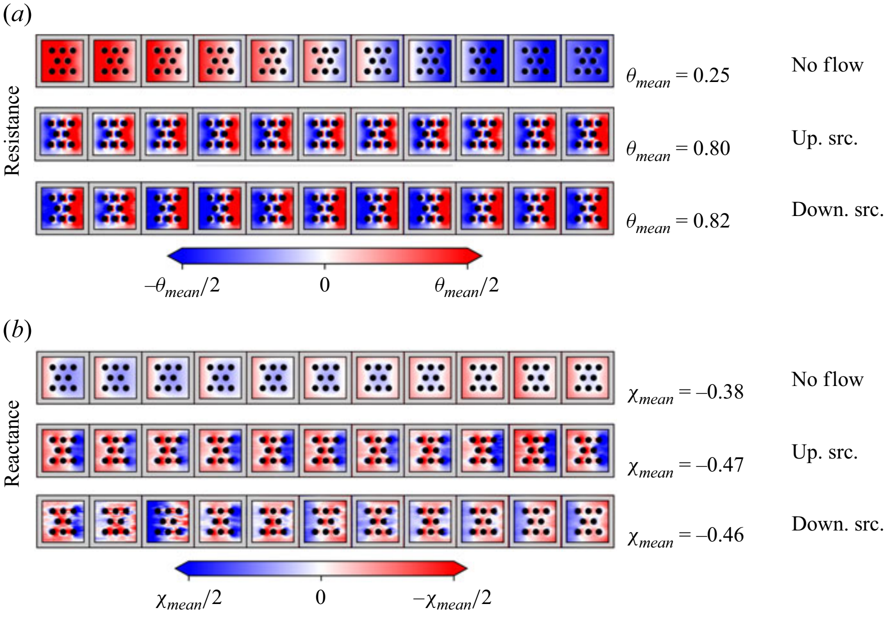

Figure 9. (*a*) Resistance and (*b*) reactance along the liner's surface obtained with *in situ* for the case with plane acoustic wave with SPL = 145 dB and $f = 1400$ Hz under three conditions: without grazing flow, with grazing flow and upstream acoustic source and with grazing flow and downstream acoustic source.

145 dB, with and without grazing flow. The SPL on the surface results from two main contributions: pressure fluctuations induced by the acoustic wave and those generated by the turbulent grazing flow. The interaction of the grazing flow with the liner's orifices affects both wall-normal and streamwise velocity fluctuations near the orifices, as will be detailed in § 5.4. This results in localised variations of the surface pressure fluctuations, which contribute to the spatial distribution of SPL shown in the figure. This might explain why the local SPL can exceed that of the imposed acoustic wave alone, consistent with the findings of Roncen (2025*a*), who emphasised that turbulence-induced pressure fluctuations cannot be neglected.

The SPL surface distributions differ from those at the channel centreline. Without grazing flow, there is an almost monotonic SPL reduction on the surface. On the other hand, in the presence of a grazing flow, there is a reduction of the SPL upstream of the orifice and an increase downstream of it, independently of the propagation direction of the acoustic wave. This trend persists across all tested frequencies and SPL levels, including the lower SPL case (130 dB), although results are omitted here for brevity. The cause of this redistribution might lie in the near-wall hydrodynamic field around the orifices.

4.2. *Surface distribution of impedance components obtained with the in situ method*

Resistance and reactance are computed using the *in situ* method as described above. The reference microphone at the backplate is always located at the centre of each cavity backplate, while the face sheet microphone is moved to generate contour plots. These contours are shown in figure 9 for an incident acoustic plane wave with SPL = 145 dB and $f = 1400$ Hz, with and without grazing flow. To highlight the location-dependent impedance, the figures display the changes in resistance and reactance relative to the mean value calculated on the entire surface.

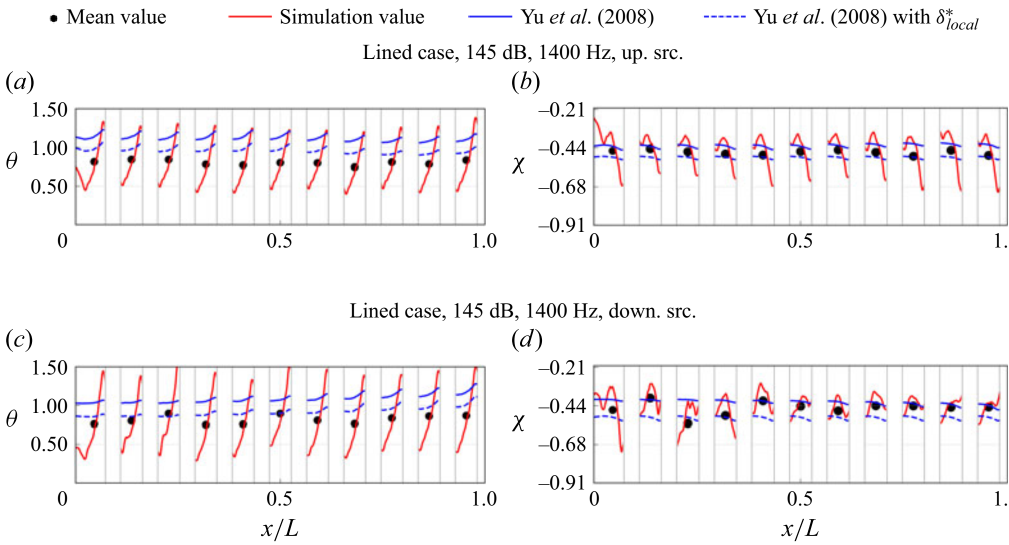

Figure 10. Streamwise distribution of resistance and reactance compared with the semi-empirical model by Yu *et al.* (2008) using different values of δ^* and the local SPL. Data shown for SPL = 145 dB and frequency of 1400 Hz. (*a*,*b*) Upstream acoustic source, (*c*,*d*) downstream acoustic source.

In the absence of the grazing flow, the resistance decreases in the propagation direction of the acoustic wave because of a reduction of the SPL. The resistance decreases along each cavity. Then, a jump in the resistance value is present when changing the cavity because the reference microphone at the backplate changes. Conversely, in the presence of a grazing flow, the spatial distribution of the resistance sees larger variations over each cavity; there is a strong reduction of the resistance when changing cavity; around each orifice, the resistance is always lower upstream of the orifice and higher downstream. The variation of resistance is up to a factor of 3, suggesting that the selection of the sampling location is crucial. This behaviour might be caused by the local surface SPL, which depends on the local amplitude of the acoustic wave and the surface pressure fluctuations altered by the presence of the orifices, as it will be described later. The pattern remains unchanged with respect to the direction of acoustic wave propagation, although the mean value over the surface slightly varies.

Data extracted at the centreline of the liner sample are shown in figure 10 for both upstream (*a*,*b*) and downstream (*c*,*d*) acoustic wave locations. In this figure, the resistance predicted using the semi-empirical model by Yu *et al.* (2008) is reported using the local SPL and the value of the boundary layer displacement thickness δ^* obtained from the smooth-wall simulation upstream of the liner and the local one obtained from the lined simulation (which will be detailed in the next section). The line plot in figure 10(*a*,*c*) highlights that the semi-empirical prediction from Yu *et al.* (2008) approaches the mean value of resistance if the local values of δ^* are used. The reason will be explained in the following.

Similar observations can be made for the reactance, for which the cavity-averaged values (black dots in the figure) weakly depend on the acoustic wave propagation direction. These results contrast with findings reported in the literature for impedance educed using model-fitting inference methods (Spillere *et al.* 2020) and may be explained by the fact that the *in sit*u approach relies on surface pressure measurements and does not employ boundary conditions to model the near-wall flow–acoustic interaction.

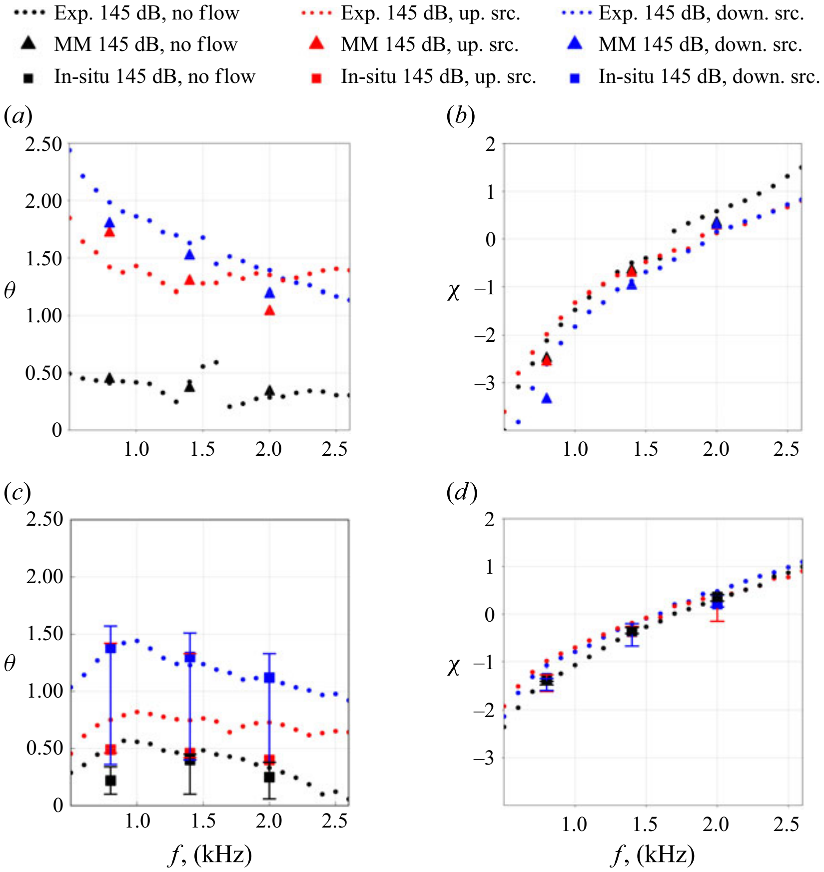

Figure 11. Comparison of (*a*,*c*) resistance and (*b*,*d*) reactance components of impedance for acoustic wave amplitude equal to 145 dB. (*a*,*b*) The MM and (*c*,*d*) *in situ* results.

These findings emphasise that the local amplitude of the acoustic and flow profile must be considered when measuring with the *in situ* method. However, the semi-empirical model does not capture the high resistance values observed in the numerical data at the beginning and end of each cavity.

4.3. *Average impedance and comparison with experimental data*

While numerical simulations allow for mapping the impedance distribution on the entire liner sample, the average value is often used to characterise the acoustic liner. Therefore, the impedance obtained using the MM method is reported in figure 11(*a*,*b*) for the cases with SPL equal to 145 dB and the three frequencies investigated, with and without grazing flow and both acoustic wave propagation directions. Experimental results from Bonomo *et al.* (2022) are also reported. In figure 11(*c*,*d*), the *in situ* results are compared with the experimental data at a similar sampling location (figure 3*b*); the bars indicate the minimum and maximum values obtained over the liner's surface. Numerical and experimental results show a reasonable agreement with similar trends. However, as pointed out above, the length of the liner sample differs between experiments and simulations, thus challenging the comparison at the lowest frequency investigated.

While the two methods yield roughly similar resistance values without flow, the resistance values obtained in the presence of flow, both in the experiments and numerical simulations, differ. The largest value obtained from the *in situ* method is lower than the average one obtained with the MM method. However, both methods show that the resistance increases with the grazing flow and is lower when the acoustic source is located upstream.

The reactance shows smaller variation with and without flow than the resistance for both techniques. This result agrees with previous findings in the literature (Spillere *et al.* 2020) and can be explained by the fact that, in the mass–spring analogy, the reactance corresponds to the balance between mass and stiffness, which is more directly related to the cavity depth than to the presence of low (Panton & Miller 1975; Jones *et al.* 2002). According to the Goodrich model (Yu *et al.* 2008) the reactance is therefore predominantly influenced by the cavity depth and by the SPL. Grazing flow affects the reactance only via the orifice end correction – i.e. the oscillating fluid volume in and around the orifice – thereby causing the observed minor variations in the reactance curve. However, the differences between cases are more evident in the results from the MM method. In particular, the MM method shows that the frequency at which the reactance is equal to zero shifts to higher values in the presence of the flow, and this does not depend on the propagation direction of the acoustic wave. This frequency shift is attributed to the flow-induced blockage effect, which effectively reduces the face sheet porosity (Tam & Kurbatskii 2000*a*). Furthermore, in the low-frequency range, the reactance values are higher for the upstream acoustic source than for the downstream one. It is important to note that the slope of the reactance curve differs between the MM and the *in situ* methods. This highlights that the educed impedance is inherently dependent on the eduction technique employed, as each method relies on distinct physical assumptions and boundary conditions.

Finally, the effect of the acoustic wave SPL is reported for the frequencies equal to 800, 1400 and 2000 Hz in figure 12. In this case, the *in situ* results are reported as the average over the entire liner surface for the sake of comparison with the MM method.

As expected, without the grazing flow, increasing the SPL results in a rise in resistance. This reflects a transition in the liner's behaviour from an almost linear to a nonlinear regime (Melling 1973; Tam & Kurbatskii 2000*b*). In the presence of flow, the resistance varies less by varying the SPL for both the MM and *in situ* techniques. Similar observations can be made for the reactance. This observation is consistent with previous findings in the literature, particularly with the trend in resistance predicted by the semi-empirical model proposed by Yu *et al.* (2008). This effect may be attributed to the increase in pressure fluctuations caused by the turbulent flow, as reported by Roncen (2025*b*), which is not accounted for in the eduction techniques. Indeed, both flow- and SPL-induced effects are primarily related to the wall-normal particle velocity; increases in turbulent fluctuations or SPL both contribute to an increase in the liner's resistance (Roncen 2025*b*).

Notably, when considering the mean resistance obtained with the *in situ* method, at the highest SPL, values in the presence of grazing flow vary less on varying the direction of propagation of the acoustic wave with respect to the ones obtained with the MM technique. This might be caused by the fact that impedance obtained from the *in situ* technique is not dependent on any flow-based boundary condition. Finally, this figure shows that for both SPLs, the surface-averaged *in situ* results are different from the MM ones.

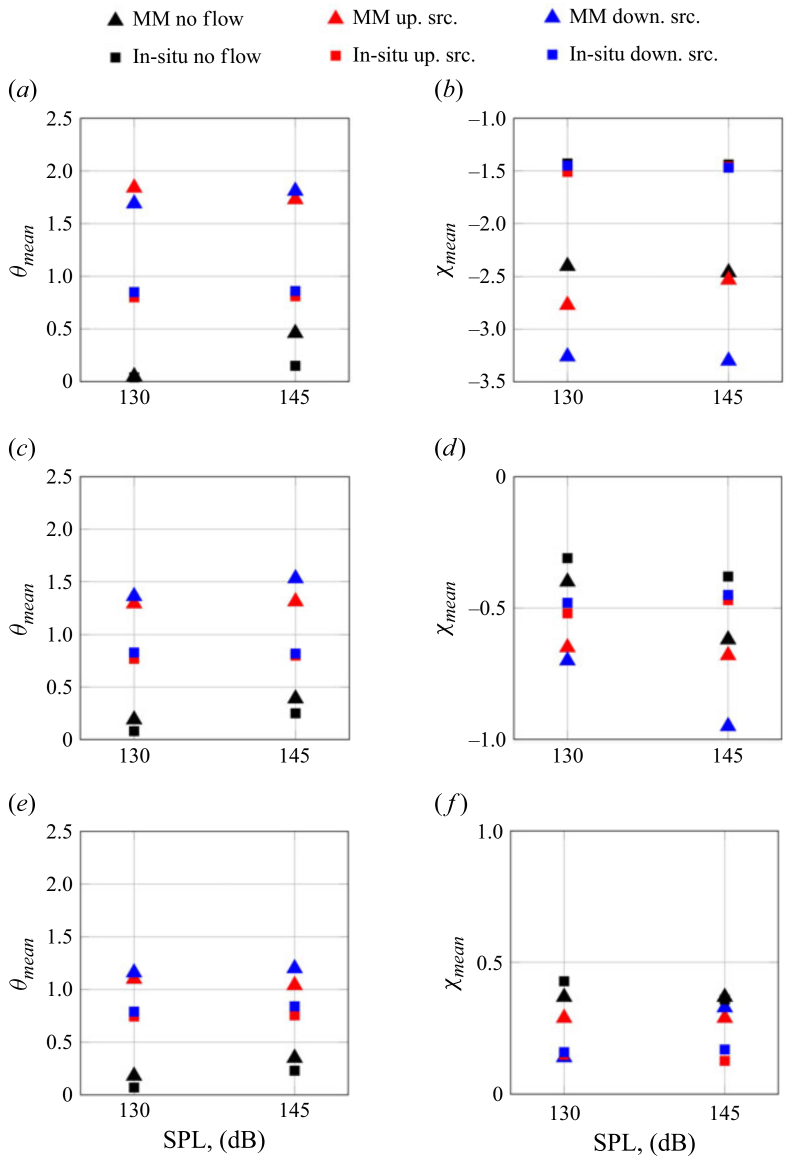

Figure 12. (*a*,*c*,*e*) Resistance and (*b*,*d*,*f*) reactance obtained from the MM and *in situ* techniques. The *in situ* results have been obtained as an average over the entire liner's surface. Results refer to a plane acoustic wave at varying SPLs, with and without grazing flow. (*a*,*b*) Incident acoustic wave with $f = 800$ Hz, (*c*,*d*) $f = 1400$ Hz and (*e*,*f*) $f = 2000$ Hz.

5. Aerodynamic results

The presence of a grazing flow influences the impedance of acoustic liners. In this section, we describe how the spatial development of the turbulent flow is affected by the transition from the solid to the acoustically treated surface, by the acoustic liner streamwise length and even by the acoustic-induced velocity fluctuations.

5.1. *Instantaneous flow*

Before digging into the mean flow quantities, a qualitative description of the instantaneous flow features is reported in figure 13. More in detail, figure 13(*a*,*b*) present the contour plots of the instantaneous streamwise velocity component, and figure 13(*c*,*d*) the wall-normal velocity component in a wall-parallel plane at $y/h = 0.003$, corresponding to $y^+ \approx 15$ in the smooth-wall case. Comparisons are made between the smooth wall and the lined surface. The streamwise velocity component exhibits low- and high-speed streaks, as for the smooth-wall case, but with higher intensity fluctuations and larger spanwise size. Higher wall-normal velocity fluctuations are observed where the liner orifices are located, caused by the flow recirculation within the orifices (Shahzad *et al.* 2023*b*). This is more evident in the wall-normal plane at $z/l = 0.5$ shown in figure 13(e,f). The higher velocity fluctuations, caused by the flow within the orifices, are not only localised close to the surface but also extend towards the centre of the duct. This suggests that the acoustic liner modifies the flow near the wall and in the outer portion of the flow.

5.2. *Mean velocity profiles*

Figure 14 compares the smooth-wall mean streamwise velocity profiles at $x/L = 0$ with the ones at three streamwise positions over the liner, $x/L = 0, 0.45$ and 1. At the beginning of the liner ($x/L = 0$), the introduction of the lined section changes the pressure gradient compared with the smooth-wall configuration, primarily affecting the outer-layer velocity profiles. The velocity profile at $x/L = 0.45$ reveals a pronounced reduction of the velocity in the wall-normal region ($10^{-2} < y/h < 5\times 10^{-2}$). The average streamwise velocity reduction in this region, relative to the inlet profile, is $\Delta U = -(U_{x/L=0.45} - U_{x/L=0})/U_{x/L=0} = 14\,\%$. This result is consistent with previous findings for turbulent flows over rough surfaces (Jiménez 2004) and acoustic liners (Shahzad *et al.* 2023*b*). The streamwise velocity near the wall continues to reduce moving at $x/L = 1$, but the rate of reduction is less strong than for the first half of the lined section ($\Delta U = -(U_{x/L=1} - U_{x/L=0.45})/U_{x/L=0.45} = 3\,\%$).

The impact of the grazing acoustic wave on the streamwise development of the channel flow is shown in figure 15. Here, the mean flow velocity profiles over the liner with acoustics are compared with those without acoustics. Each column reports a streamwise location, moving downstream from left to right. Each row describes the impact of a different parameter of the acoustic wave. At the beginning of the lined section, $x/L = 0$, the grazing acoustic waves weakly affect the mean velocity profiles, independently of the SPL (figure 15*a*), the frequency of the plane wave (figure 15*d*), and the propagation direction of the acoustic wave (figure 15*g*). The acoustic waves modify the velocity profile in the region in the range $0.01 < y/h < 0.04$; these differences are more evident, even if weak, i.e. $\Delta U < 4\,\%$, when increasing the SPL and near the resonance frequency of the liner, estimated without flow. Furthermore, the upstream acoustic source causes a slightly higher velocity deficit with respect to the downstream case.

The most relevant impact of the acoustic waves on the mean flow is found at $x/L = 0.45$. Here, the mean flow profile varies depending on the characteristics of the acoustic wave. The trends are similar to those found at $x/L = 0$ but enhanced. The observed dependence on the excitation frequency may be explained by the different proximity of the excitation to the liner's resonance frequency in the presence of grazing flow (figure 11). The dependency on the propagation direction is more evident at this streamwise location, with a larger velocity deficit for the upstream source.

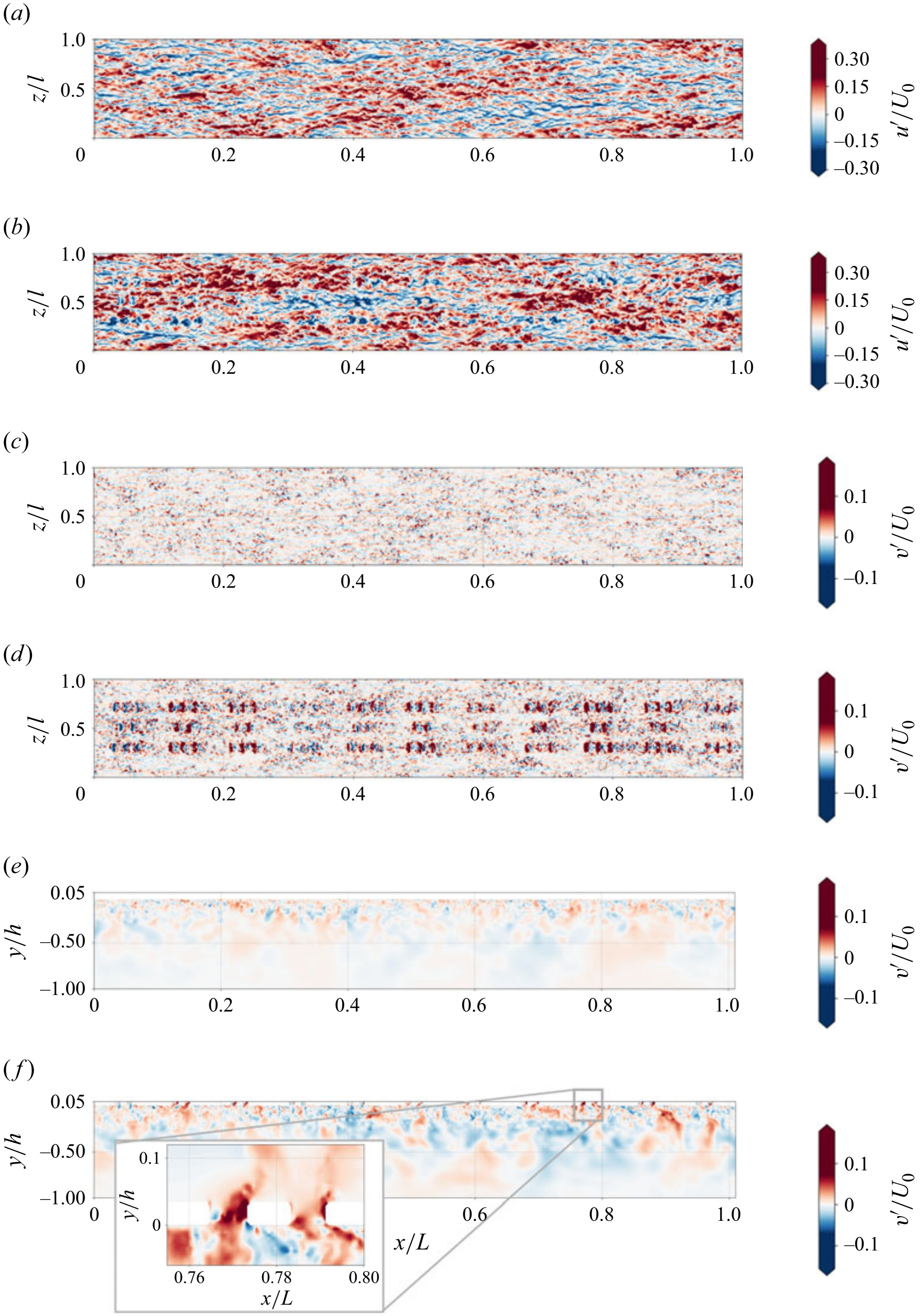

Figure 13. (*a*,*b*) Instantaneous streamwise u' (*c*,*d*) and wall-normal v' velocity components at $y/h = 0.003$. (*e*,*f*) Instantaneous vertical velocity v' component at $z/l = 0.5$. (*a*,*c*,*e*) Represent the smooth-wall case while (*b*,*d*,*f*) represent the lined-wall case. All figures show the lined-wall case without incident sound.

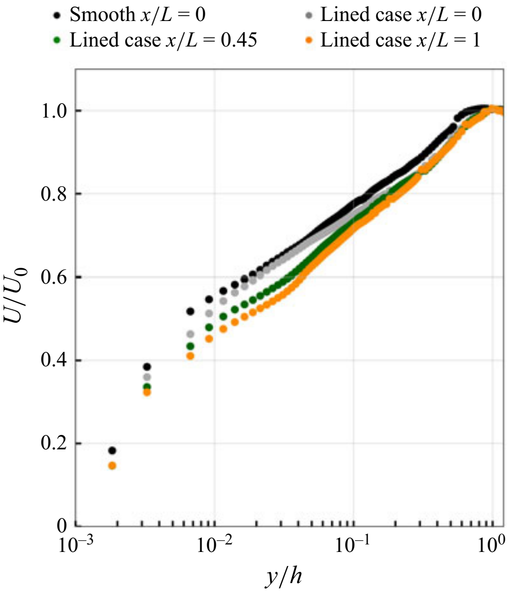

Figure 14. Time average of streamwise velocity profile in outer coordinates sampled at three locations over the liner compared with the smooth case. No incident sound wave.

At the end of the lined section, the mean velocity profiles do not depend on the characteristics of the plane acoustic wave. This might be due to the flow recovering immediately from the perturbations caused by the acoustic-induced field.

5.2.1. *Streamwise distribution of the boundary layer integral quantities*

Previous analyses have shown that the presence of the liner affects the mean streamwise velocity profiles in the region $10^{-2} < y/h < 5\times10^{-2}$. To investigate this effect in more detail, the streamwise evolution of the boundary layer thickness δ and the boundary layer displacement thickness δ^* is described. The two quantities are defined as

$$U(y=\delta) = 0.99U_0, \tag{5.1}$$

$$\delta^* = \int_0^h \left(1 - \frac{U(y)}{U_0}\right) \mathrm{d}y. \tag{5.2}$$

The boundary layer thickness, in this context, is used to measure the impact of the liner on the velocity profile. The reasons are: (i) the flow within the channel is not symmetric with respect to the centreline because the acoustic liner is present only on one side; (ii) the flow is not yet fully developed, as also happens in the reference experiment. However, since δ, is by definition an arbitrary quantity, we quantified also the streamwise variation of the displacement thickness δ^*, which better indicates near-wall flow gradients and is an important parameter for characterising the flow profile in the semi-empirical models used for computing impedance (Nayfeh *et al.* 1974; Yu *et al.* 2008). These quantities are reported in figures 16 and 17 and are made non-dimensional with respect to the corresponding value for the smooth wall at $x/L = 0$.

The streamwise development of δ in the smooth-wall case (figure 16) confirms that the flow is not yet fully developed in the lined section. As a matter of fact, δ shows a plateau from $x/L \approx 0.75$. The presence of the liner increases δ by approximately 25 %. The streamwise development of δ varies weakly when the acoustic wave is present. It is

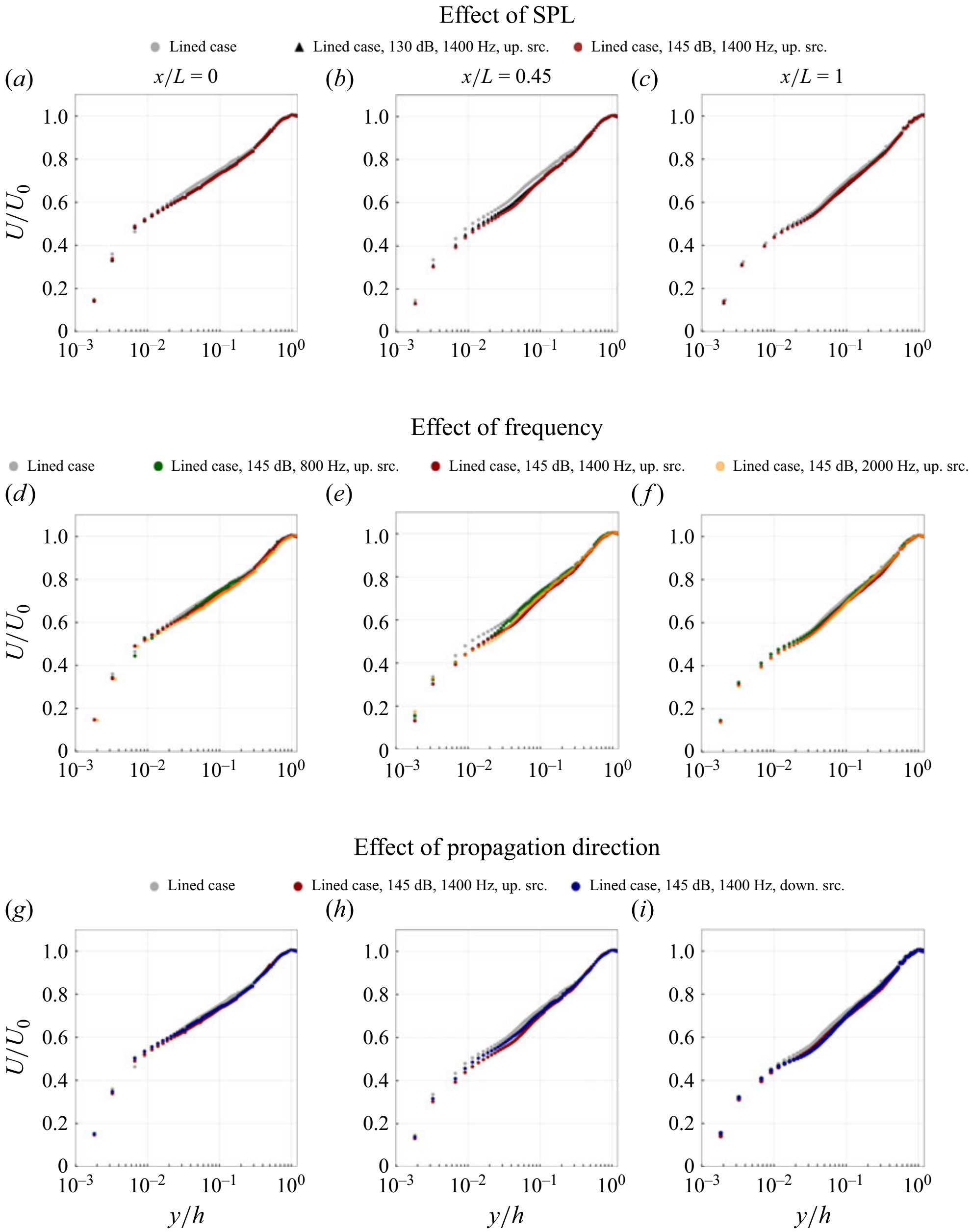

Figure 15. Time-averaged velocity profiles sampled at (*a*,*d*,*g*) $x/L=0$, (*b*,*e*,*h*) $x/L=0.45$ and (*c*,*f*,*i*) $x/L=1$. The impact of the plane wave properties: (*a*,*b*,*c*) SPL, (*d*,*e*,*f*) frequency and (*g*,*h*,*i*) propagation direction of the acoustic wave is described.

interesting to notice that the effect of the SPL, frequency and direction of the acoustic waves are visible up to $x/L \approx 0.8$ or $x/\delta_{smooth} \approx 10$. Beyond this point, the curves tend to converge, suggesting that the influence of the acoustic perturbation may diminish once the turbulent flow starts adapting to the lined surface. The weak dependence of δ on the features of the acoustic wave aligns with the previous observations (figure 15) that the presence of the acoustic liner dominates the mean flow variation.

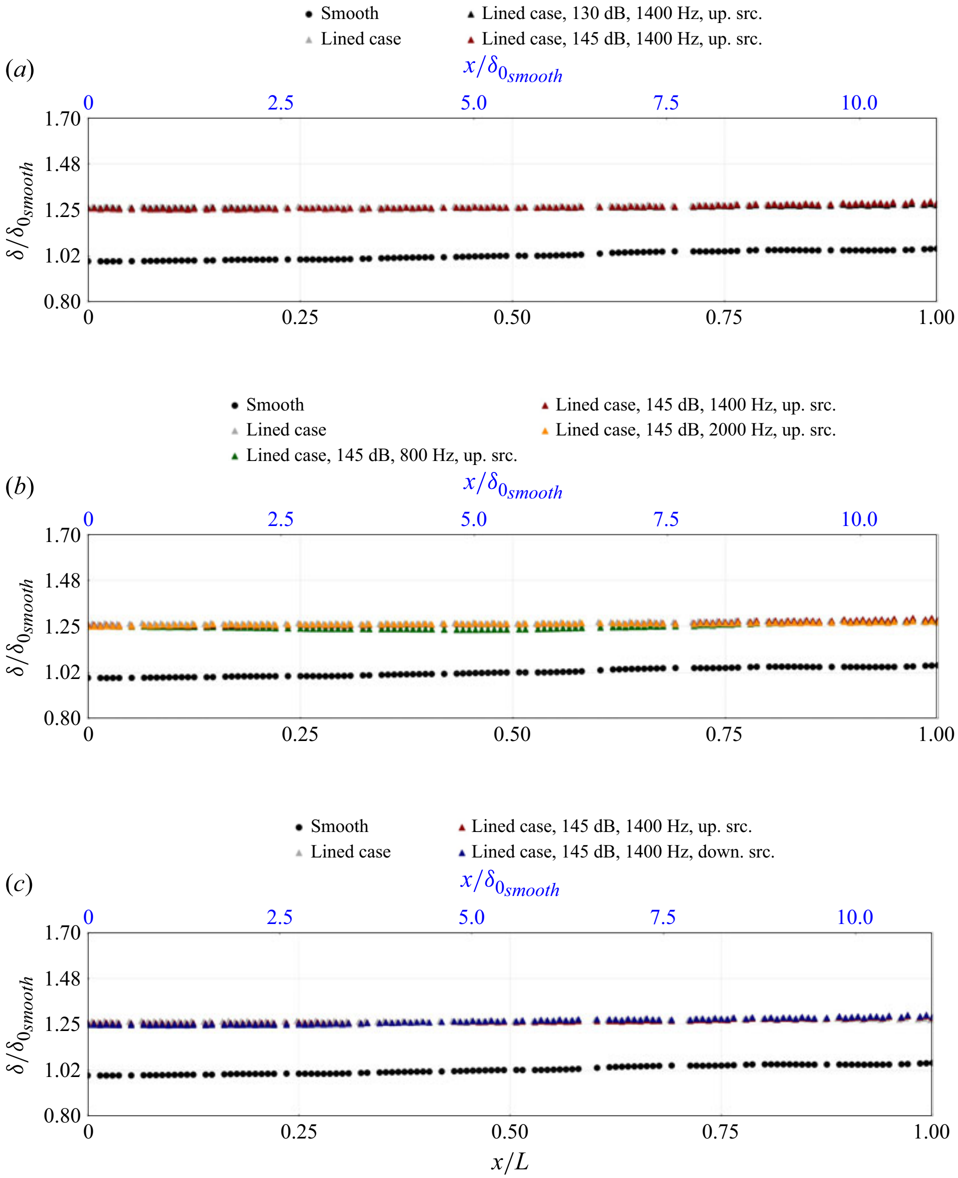

Figure 16. Streamwise development of δ over the liner. (*a*) Effect of acoustic waves' amplitudes at a fixed frequency of 1400 Hz; (*b*) effect of the acoustic waves' frequency at a fixed amplitude of 145 dB; (*c*) effect of different propagation directions at a fixed frequency of 1400 Hz and amplitude of 145 dB.

The streamwise development of δ^* (figure 17) shows a more pronounced increase with respect to the smooth wall up to 30 % and depends on the features of the acoustic plane wave. More in detail, it increases in the presence of the acoustic wave, it grows more with higher SPL (figure 17*a*), at frequencies close to the resonance frequency of the liner (figure 17*b*) and it depends on the propagation direction of the acoustic wave (figure 17*c*). In contrast to δ, δ^* emphasises the differences between upstream and downstream acoustic waves. This behaviour highlights the influence of wave direction on near-wall velocity deficit.

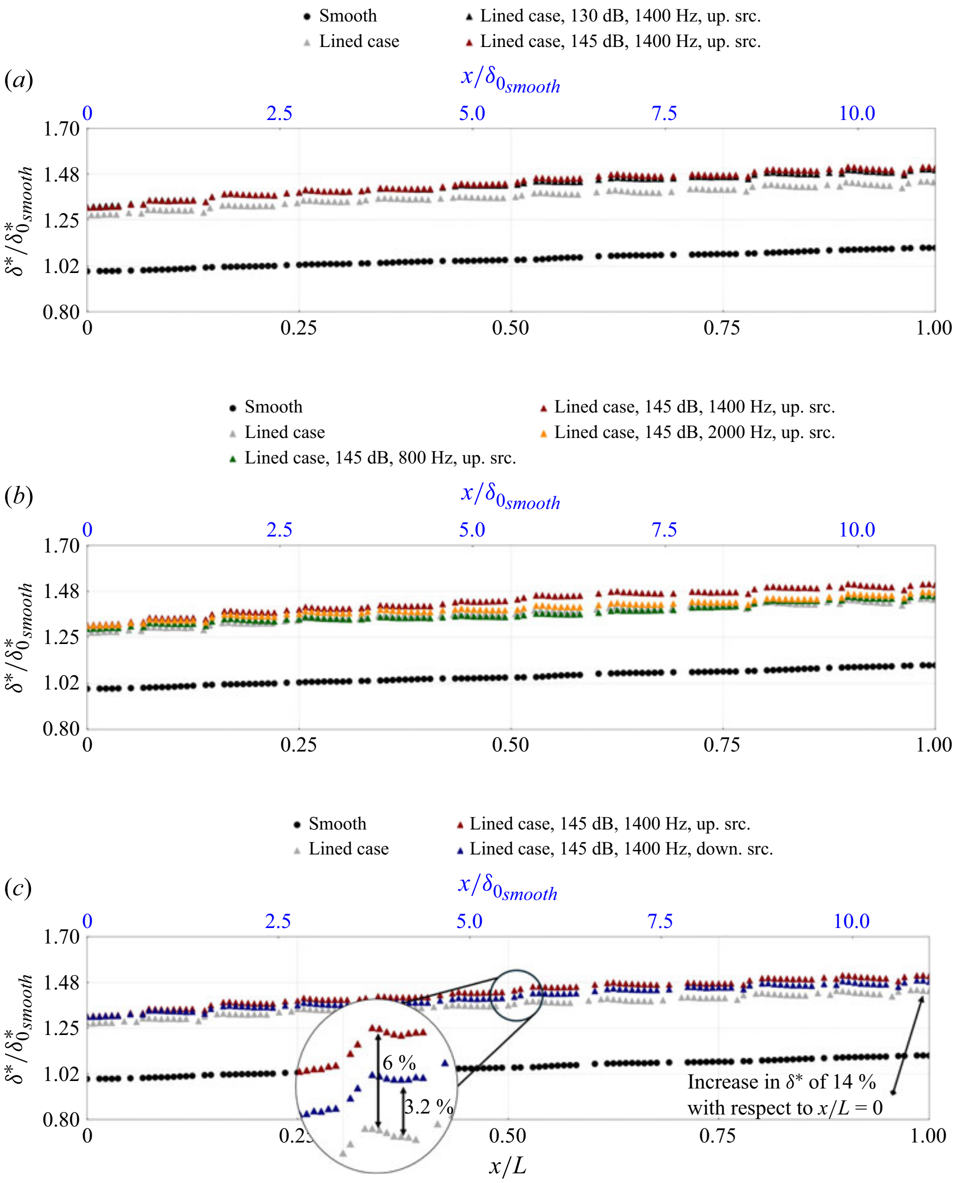

Figure 17. Streamwise development of δ^* over the liner. (*a*) Effect of different acoustic waves' amplitude at a fixed frequency of 1400 Hz; (*b*) effect of acoustic waves' frequency at a fixed amplitude equal to 145 dB; (*c*) effect of different propagation directions at a fixed frequency of 1400 Hz.

The step-like behaviour of δ^*, in correspondence with each cavity of the acoustic liner, is due to the near-wall flow modifications induced by the orifices. This effect is further enhanced by the acoustic-induced flow field. These flow features will be visualised and described in the next section.

5.3. *Impact of flow development on the near-wall and in-orifice flow field*

The observed changes in boundary layer integral parameters are driven mainly by the presence of the liner. The introduction of the acoustic liner modifies the near-wall flow,

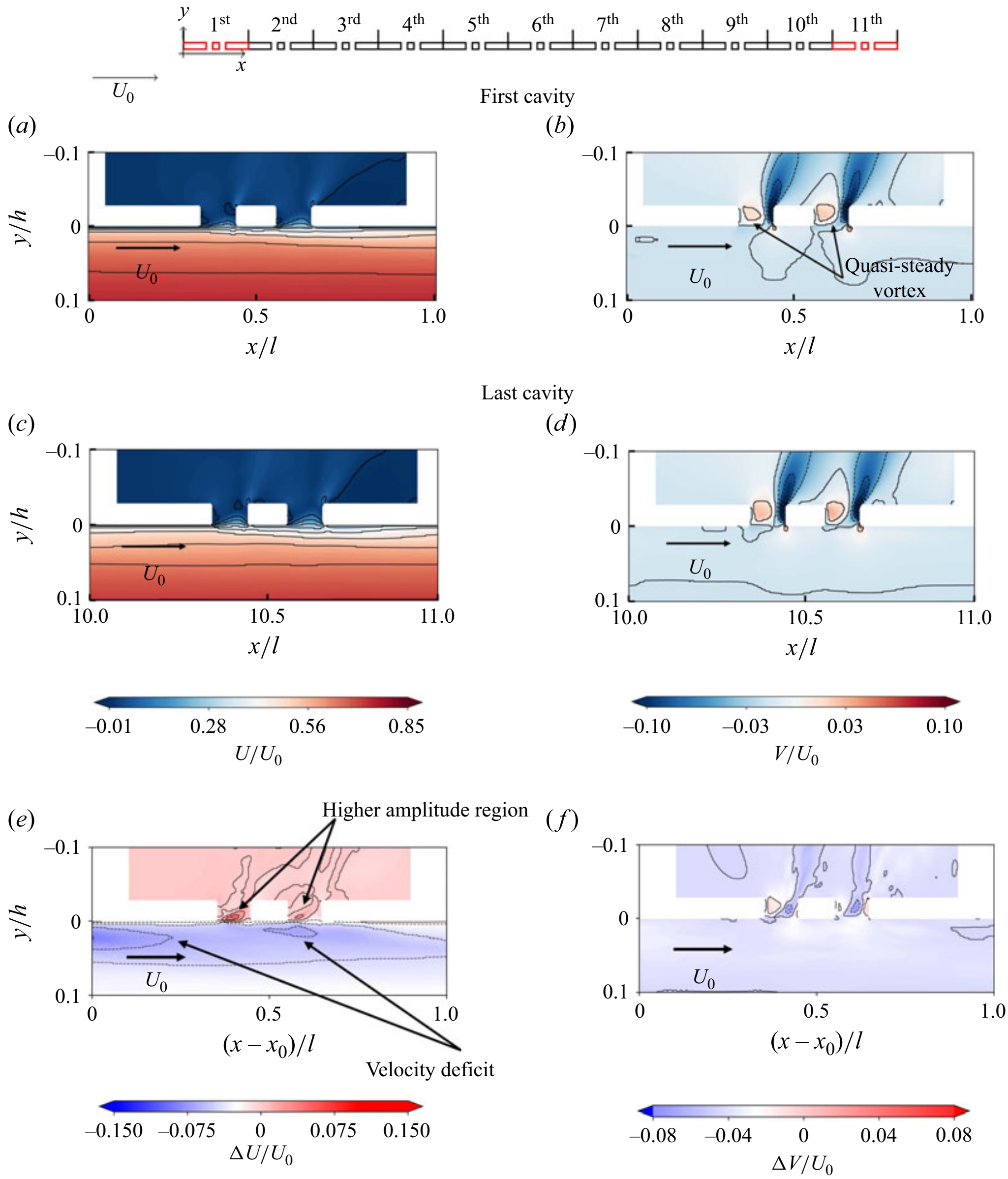

Figure 18. Contour of mean velocity component (*a*,*c*) and wall-normal velocity component (*b*,*d*) for the flow-only case. (*a*,*b*) First cavity, (*c*,*d*) last cavity. (*e*) Difference in the streamwise velocity defined as $\Delta U = (U_{last\ cav.} - U_{first\ cav.})$. (*f*) Difference in the wall-normal velocity defined as $\Delta V = (V_{last\ cav.} - V_{first\ cav.})$. All results refer to the lined-wall case without acoustic sources.

which is reflected in an increase in the boundary layer displacement thickness. To further investigate this aspect, figure 18 presents contour plots of the streamwise and wall-normal velocity components at the first and last cavities in the absence of an acoustic plane wave.

In both cavities, the wall-normal velocity contours reveal a quasi-steady vortex occupying the upstream portion of each orifice, consistent with earlier observations (Tam & Kurbatskii 2000*b*; Avallone *et al.* 2019). The vortex strength, however, slightly differs between cavities and between successive orifices. Looking at streamwise velocity

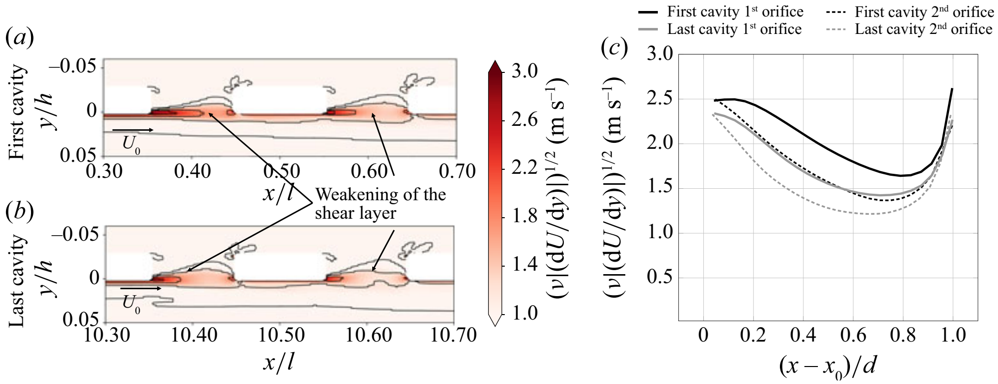

Figure 19. Contour of $\nu(|\mathrm{d}U/\mathrm{d}y|)^{1/2}$ for (*a*) the first and (*b*) the last cavities for the flow-only case. (*c*) Line plots of $\nu(|\mathrm{d}U/\mathrm{d}y|)^{1/2}$ sampled at $y/h=0$ above the orifices, comparing the first and last cavities and highlighting the downstream weakening of the shear layer. Plots show the case without incident sound waves.

components over the two cavities (figure 18*a*,*c*), for both cases, downstream of the orifices, the flow is first displaced away from the wall and then tends to reattach. The displacement in the downstream direction causes a reduction of the near-wall streamwise velocity gradient from the most upstream to the most downstream location. This is quantified in figure 18(*e*) where the difference between the flow field over the cavities is quantified as $\Delta U = (U_{last\,cav.} - U_{first\,cav.})$. Over the last cavity, near the wall, the velocity decreases by up to 12 % of U_0. As a consequence, over the orifices, the streamwise velocity component gradient in the wall-normal direction $\mathrm{d}U/\mathrm{d}y$ is also less strong for the most downstream cavity, thus resulting in localised high amplitude $\Delta U/U_0$ regions within the orifice of approximately 10 %. The latter might affect the strength of the quasi-steady vortex that is formed within each orifice, as suggested by an increase in the wall-normal velocity in the upstream part of the last cavity's orifice by $\Delta V = V_{last\,cav.} - V_{first\,cav.} = 0.03\,U_0$ (figure 18*f*).

To quantify this effect, figure 19 examines the local shear-related scale $(\nu|\mathrm{d}U/\mathrm{d}y|)^{1/2}$, which has the same units as the friction velocity, for the first and last cavities in the flow-only configuration. The contours reveal a streamwise attenuation of shear intensity over the orifice in the downstream direction, as clearly shown in figure 19(*c*), which presents this quantity at $y/h=0$. In the first cavity, the upstream orifice exhibits the strongest shear layer; at the downstream orifice, the magnitude is roughly halved, and the high-intensity shear region extends less far downstream. This trend is even more pronounced in the last cavity: the shear over its first orifice is already weaker than that in the first cavity, and it diminishes sharply over the second orifice. Moreover, $\nu(|\mathrm{d}U/\mathrm{d}y|)^{1/2}$ over the last cavities experiences a reduction in magnitude of up to approximately 30 % compared with the first cavity. The stronger shear layer at the first cavity obstructs the penetration of the acoustic wave into the orifice with respect to what happens at the last cavity. This variation can be interpreted as a spatial asymmetry in the flow field, caused by the growth of the boundary layer displacement thickness. The acoustic wave propagating in the direction opposite to the mean flow will see different near-wall flow gradients and different shears over the orifices with respect to the wave which propagates in the same direction as the flow. Furthermore, the development of the flow highlights the relevance of near-wall flow features and the need to correctly account for the boundary layer displacement thickness.

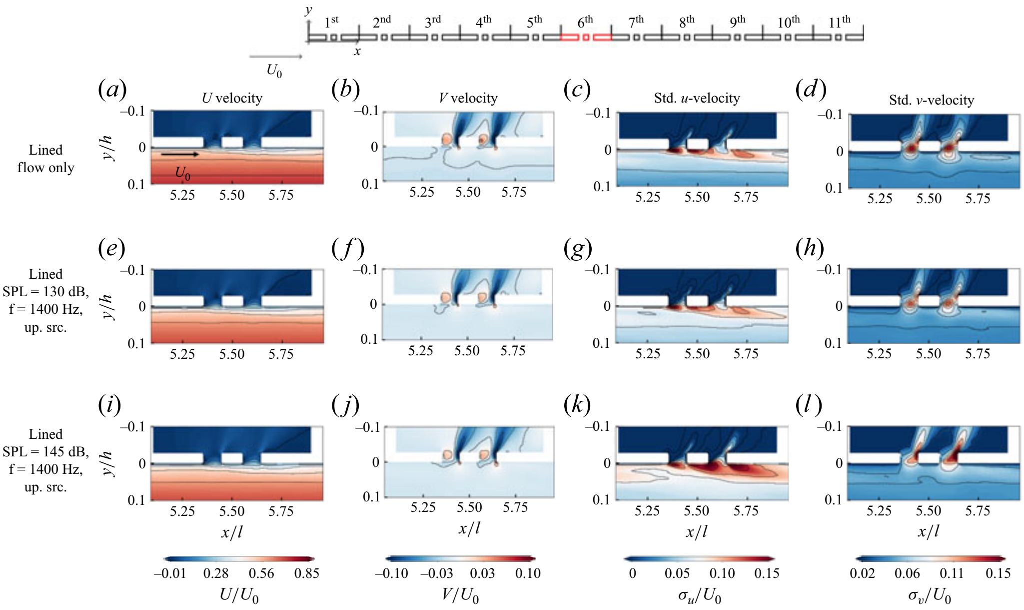

Figure 20. Contour of the mean and standard deviation of the streamwise and wall-normal velocity components for the cases: flow only, lined (*a*,*b*,*c*,*d*), flow and upstream acoustic source with SPL = 130 dB and $f = 1400$ Hz (*e*,*f*,*g*,*h*) and flow and upstream acoustic source with SPL = 145 dB and $f = 1400$ Hz (*i*,*j*,*k*,*l*).

5.4. *Impact of SPL on the near-wall and in-cavity flow field*

The preceding analysis demonstrated that the streamwise development of the grazing flow alters the near-wall and in-orifice velocity fields, primarily through a progressive reduction in the streamwise velocity gradient and weakening of the shear layer over the downstream orifices. These modifications influence the vortex dynamics and flow penetration within the cavities, even in the absence of acoustic excitation. To further understand the coupling between fluid dynamics and acoustics, this section describes how the amplitude of the acoustic wave affects the mean and fluctuating flow fields in the vicinity of the orifices. Analyses were conducted for the sixth cavity (i.e. $x/L = 0.45$).

Figure 20 presents the contours of the mean streamwise and wall-normal velocity components, along with their standard deviations. The case with acoustic excitation is compared with the case without acoustic excitation. In the absence of acoustic waves (figure 20*a*–*d*), the contour of the standard deviation of the streamwise velocity component σ_u/U_0 (figure 20*c*) highlights the presence of high-intensity fluctuations over the first orifice and after the second one. These fluctuations are caused by vortices shed near the wall, which are also responsible for the displacement of the flow away from the wall. On the other hand, the turbulent flow causes high-intensity fluctuations of the vertical velocity component σ_v/U_0 (figure 20*d*) at the centre of the orifice and the downstream edge of the face sheet. The location of the peak displaces slightly upstream in the second orifice with respect to the first one.

The presence of acoustic waves, with only one frequency reported for the sake of conciseness, weakly alters the mean flow, but largely the velocity fluctuations, as can be seen by comparing figures 20(*c*) and 20(*m*). As the amplitude of the acoustic wave increases, the flow is progressively displaced away from the wall, a behaviour analogous to what occurs in turbulent boundary layers subjected to wall-normal blowing or flow

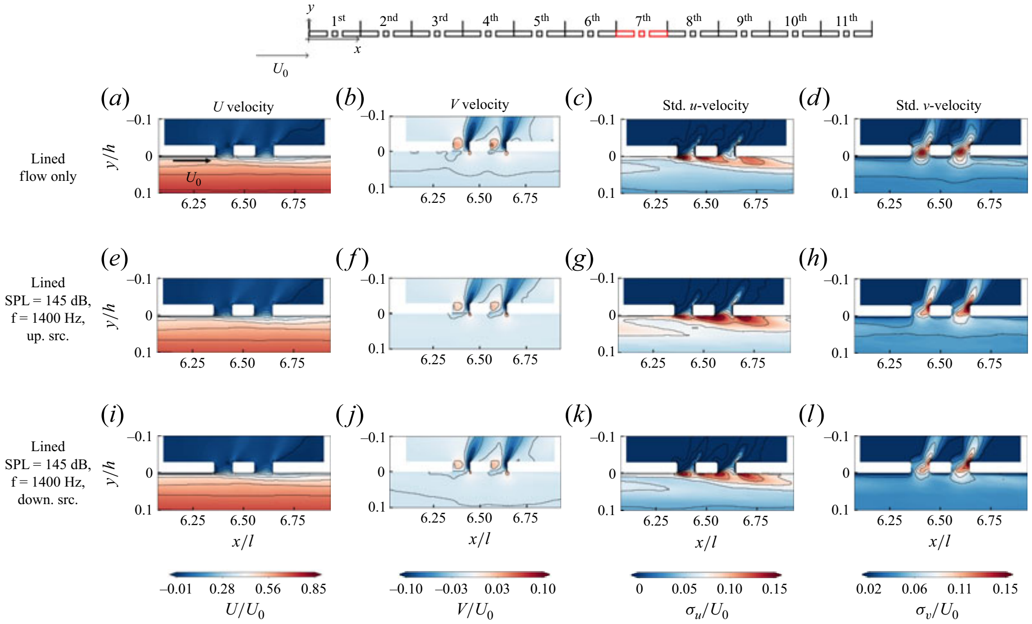

Figure 21. Contour of the mean and standard deviation of both the streamwise and the wall-normal velocities for the cases: flow only, lined (*a*,*b*,*c*,*d*), flow and upstream acoustic source with SPL = 145 dB and $f = 1400$ Hz (*e*,*f*,*g*,*h*) and flow and downstream acoustic source with SPL = 145 dB and $f = 1400$ Hz (*i*,*j*,*k*,*l*).

over permeable surfaces (Jiménez 2004; Zhang & Bodony 2016; Avallone *et al.* 2019; Spillere *et al.* 2020). This results in a stronger velocity deficit near the wall and elevated streamwise fluctuations in the outer layer. Increasing the SPL to 145 dB, the amplitude of the streamwise velocity fluctuations near the wall increases; σ_u/U_0 shows a large amplitude further away from the wall, which increases at the downstream orifice. Also, σ_v/U_0 varies substantially with respect to the other two cases; the peak of σ_v/U_0 is localised at the downstream edge of both orifices, and it increases in amplitude at the more downstream edge.

5.5. *Impact of different directions of propagation of the acoustic wave*

This section investigates how the propagation direction of the acoustic wave affects the flow field. To isolate this effect, the mean velocity field is analysed at $x/L = 0.54$, corresponding to the seventh cavity. Here, the incident SPL is the same for both directions (SPL $\approx$ 137 dB), yet the displacement thickness still differs by $\approx 3\,\%$.

Contours of the time-averaged and standard deviation of both the streamwise and wall-normal velocity components are shown in figure 21 for the cases: flow only, flow and upstream acoustic source and flow and downstream acoustic source. Only the case with acoustic plane wave amplitude equal to 145 dB and $f = 1400$ Hz is reported for the sake of conciseness, because similar observations can be made for the other cases.

The propagation direction of the acoustic wave with respect to the mean flow has a minor impact on the time-averaged flow field when the local amplitude of the acoustic wave is similar. Contours of U/U_0 and V/U_0 do not show relevant differences between the two cases. The only visible difference is that, downstream of the second orifice, the flow is slightly less displaced away from the wall when the acoustic wave propagates in the opposite direction to the mean flow, which is consistent with the δ^* evolution (figure 17*c*).

The strong similarities between the two cases explain the previous observation that the mean flow is affected more by the presence of orifices than by the acoustic field. However, the propagation direction of the acoustic wave has more impact on the amplitude of the velocity fluctuations than on their spatial distribution. For the upstream acoustic source, σ_u/U_0 is higher, and the region with high amplitude extends spatially further downstream and away from the wall than in the case with a downstream source. This might be caused by the convective nature of the flow that tends to drag downstream the velocity fluctuations induced by the acoustic-induced velocity within the orifice. For the downstream acoustic source, by contrast, it appears that the regions with high amplitude velocity fluctuations are confined near the wall.

The direction of propagation of the acoustic wave also impacts the amplitude of the vertical velocity fluctuations within the orifice. As illustrated in figure 22, the peak of σ_v/U_0 shifts towards the downstream edge of each orifice and penetrates deeper into the cavity when acoustic forcing is present. For the cases with acoustics, the peak value nearly doubles at $y/\tau=-1$ compared with the flow-only case. The distribution remains topologically similar for the two cases. Therefore, it can be concluded that, at similar SPL, the wave direction weakly alters the spatial distribution of the in-orifice flow fluctuations but modulates their intensity. The larger amplitude of the velocity fluctuations observed in the upstream-propagating wave case may be linked to the different boundary layer displacement thicknesses.

5.6. *Streamwise evolution of the standard deviation of the velocity fluctuations*

To assess how the liner surface geometry and acoustic forcing influence the outer layer of the turbulent flow, the standard deviations of the streamwise and wall-normal velocity components are examined at six streamwise stations along the liner, as shown in figure 23. The analysis focuses on cases with a fixed excitation frequency of 1400 Hz, and varying SPLs and propagation directions. Results are compared against both the flow-only and smooth-wall baselines. Similar trends were observed at other frequencies and are omitted here for brevity.

At $x/L=0$ (station 1), no appreciable differences are observed in the streamwise velocity standard deviation profiles between the smooth-wall and lined configurations. Similarly, acoustic forcing has no discernible effect on the flow when applied over a smooth wall. In contrast, the wall-normal velocity fluctuations exhibit a slight increase in the region $10^{-2}<y/h<1$ compared with the smooth-wall case. However, differences become more visible at the second streamwise station ($x/L=0.45$) where the lined flow-only case exhibits a distinct hump at $y/h\approx 4\times 10^{-2}$. This outer-layer peak is consistent with previous observations of zero-pressure-gradient (ZPG) turbulent boundary layers over porous or perforated surfaces, where wall-normal transport promotes the formation of secondary motions (Scarano, Jacob & Gowree 2024). The hump at $y/h\approx 4\times 10^{-2}$ is amplified by the presence of the acoustic wave. The amplitude of the hump increases as the amplitude of the acoustic wave increases, and when the acoustic wave propagates as the mean flow does. For the case with the acoustic wave propagating in the direction opposite to the mean flow, no difference is visible with respect to the flow-only case. This is because the amplitude of the acoustic wave at this location has decreased to approximately 130 dB (figure 7). Closer to the wall, almost no variation is found with respect to the smooth-wall case. Considering the standard deviation of the wall-normal velocity component, a similar conclusion can be drawn. Specifically, an increase in σ_v/U_0 is observed at the same wall-normal location ($y/h\approx 0.04$), consistent with the upward displacement of fluid from the near-wall region toward the outer layer. This displacement becomes more pronounced

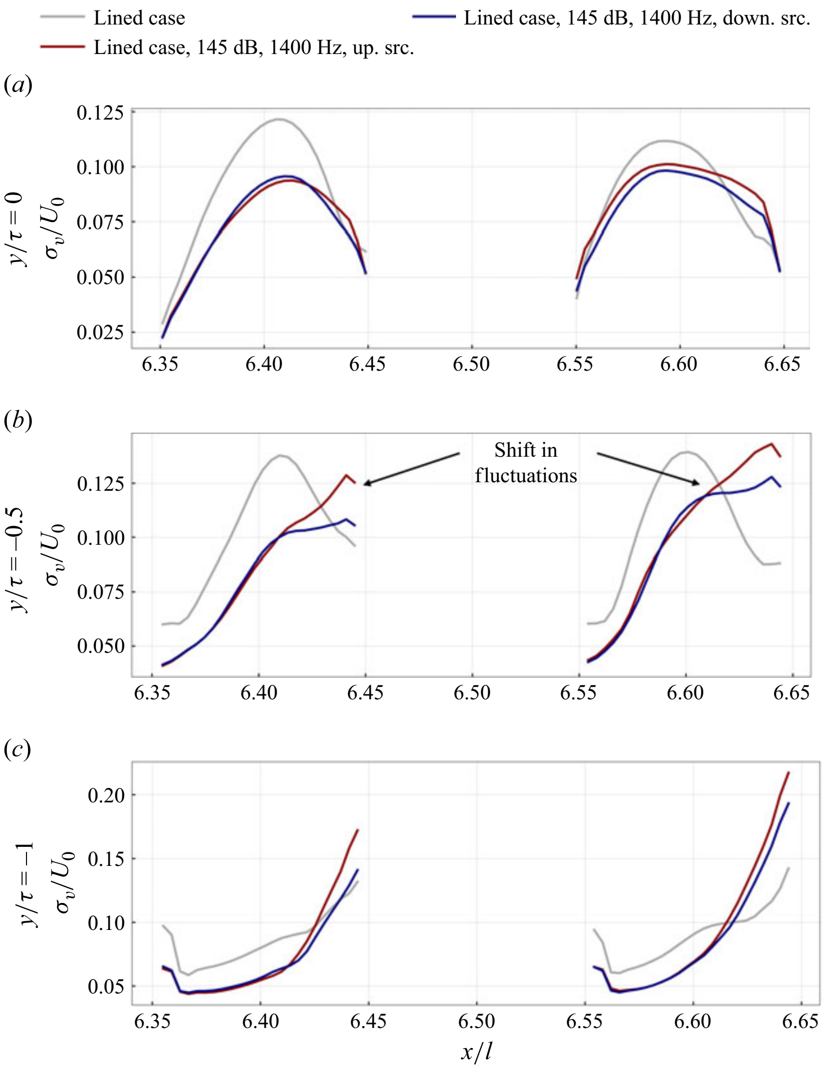

Figure 22. Spatial distribution of σ_v/U_0 into two adjacent orifices of the seventh cavity at (*a*) $y/\tau = 0$, (*b*) $y/\tau = -0.5$, (*c*) $y/\tau = -1$. Lined flow-only case, flow and acoustics with SPL = 145 dB $f = 1400$ Hz and upstream acoustic source, SPL = 145 dB $f = 1400$ Hz and downstream acoustic source.

in the case with an upstream acoustic source at SPL = 145 dB, highlighting the role of acoustic forcing in enhancing momentum exchange and vertical transport within the near-wall flow. At $x/L = 0.73$ (i.e. the third streamwise station), the outer peaks of both the streamwise velocity and wall-normal velocity variance are enhanced with respect to the smooth-wall case. At this station, for both the streamwise and wall-normal velocity, it is more difficult to spot differences in the outer hump amplitude between the cases with varying both the amplitude and direction of the acoustic wave, meaning that the effect of the acoustic is less evident. The reason behind this behaviour is believed to be driven by two different causes: (i) the acoustic wave is attenuated when progressing over the liner, (ii) the turbulent flow is adapting to the change in the surface. This is further supported by the standard deviation profiles at station 4. As a matter of fact, at this location, almost no differences are found in the amplitude of the outer hump. The turbulent flow seems

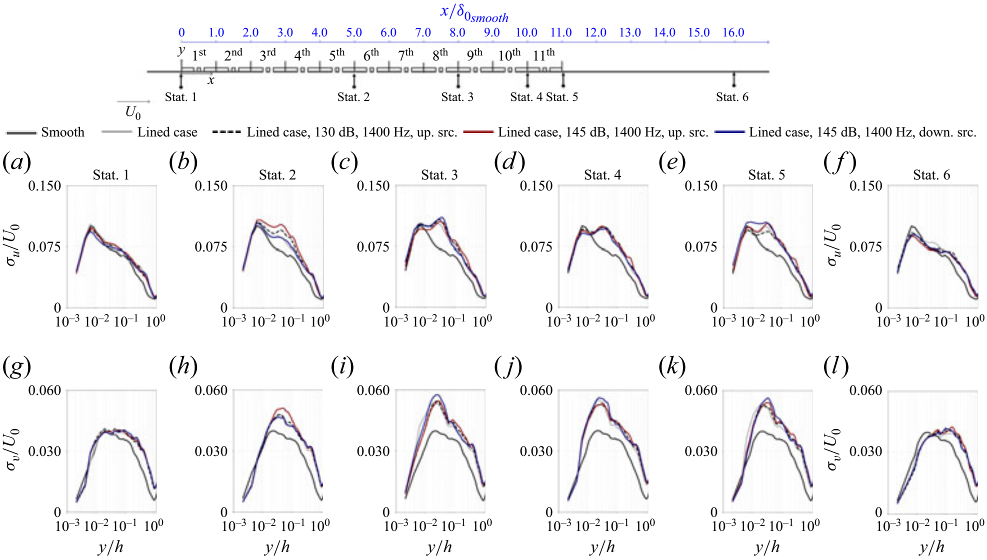

Figure 23. Streamwise velocity standard deviation (top row) and wall-normal velocity standard deviation (bottom row) for the different test cases reported in the legend.

to be adapted to the lined surface. Even though the phenomenology of the set-up under investigation slightly differs from a ZPG turbulent boundary layer, the behaviour of the flow over the lined surface resembles the behaviour of turbulent flow over rough surfaces, where outer-layer features stabilise further downstream (Jaiswal & Ganapathisubramani 2024). A slight reduction in the inner peak amplitude is also observed, consistent with earlier studies of turbulent flow over acoustic liners (Shahzad *et al.* 2023*a*), and this inner-layer attenuation is modestly modulated by the acoustic forcing.

At $x/L = 1.0$ (station 5), the flow encounters a sudden transition from the lined surface to a smooth wall. Here, the outer-layer hump is modulated once again by the amplitude and direction of the acoustic wave. The largest deviation from the lined flow-only case is found in the downstream case at SPL = 145 dB. This region is characterised by the formation of secondary motions induced by the abrupt surface change, which are further intensified by the acoustic forcing. As a result, both streamwise and wall-normal velocity fluctuations show increased amplitude modulation by the acoustic wave properties.

Finally, at the most downstream location, $x/L = 1.5$, where the smooth condition is recovered downstream of the liner, variance profiles for both wall-normal and streamwise velocity components resemble the ones for the smooth wall. This indicates that after the surface transitions back to a smooth one, the flow tends to recover to a canonical state, regardless of whether acoustic forcing is present or not.

6. Acoustic-induced velocity and mass flow rate

6.1. *Acoustic-induced velocity field within the orifices*

Building on the previous findings, it is evident that the combined effects of the lined surface and acoustic excitation influence both the time-averaged and fluctuating flow fields near the wall. These modifications, in turn, alter the flow dynamics within the orifices. The behaviour of the flow in and around the orifices might serve as a direct indicator of acoustic energy dissipation. In this section, details of the acoustic-induced velocity within the orifices are described. For this purpose, the acoustic-induced velocity fields have been

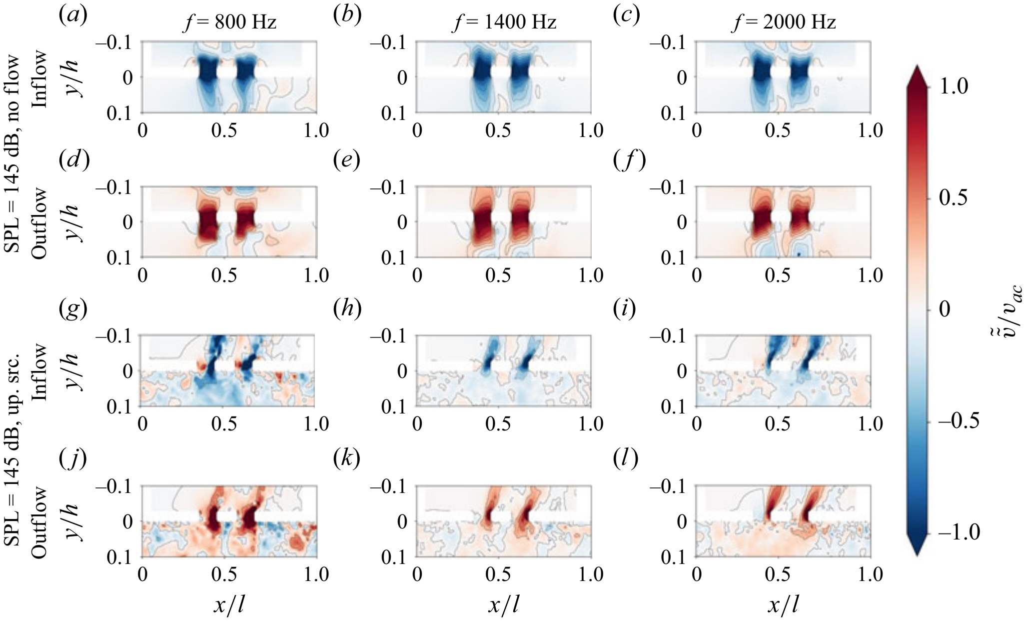

Figure 24. Contour plots of the acoustic-induced velocity at the peak of the inflow phase and peak of the outflow phase. All cases have an incident sound with amplitude equal to 145 dB and the three frequencies analysed.

obtained using the triple value decomposition approach described in § 2. They are shown in figure 24 for the case with SPL equal to 145 dB and for the three frequencies. For each case, the inflow and outflow phases are shown, corresponding to the maximum and minimum velocity within the upstream orifice.

The reconstructed velocity is normalised by the theoretical acoustic velocity proposed by Morse, Ingard & Morse (1968) as done in previous studies (Zhang & Bodony 2016; Léon *et al.* 2019), even if valid in the absence of grazing flow

$$v_{ac}^{*}=\frac{|p'|}{\rho\omega(\tau+0.8d)}\frac{1}{\sqrt{\left[\left(\dfrac{\omega_H}{\omega}\right)^2-1\right]+\left(\dfrac{\omega_H}{\omega Q}\right)^2}}, \tag{6.1}$$

where p' is the pressure fluctuation, obtained from the SPL, ω and ω_H are the forcing and resonant frequency, Q is the quality factor and ρ is the density. A constant value of $Q=7$ was used for both the no-flow and flow conditions. This value was determined as the best fit to match the acoustically induced velocity in the no-flow case, resulting in velocity values of 6.76, 23.66 and 12.37 m s^{-1} for acoustic wave amplitudes of 145 dB at frequencies of 800, 1400 and 2000 Hz, respectively.

In the absence of grazing flow, the velocity contours exhibit a slightly asymmetric spatial distribution for all frequencies and for both the inflow and outflow phases. The asymmetry concerning the centre of the orifice $x/d=0$ is due to the grazing acoustic wave causing a flow reversal region near the upstream edge. This is true for both the inflow and outflow cases. Additionally, the orifices exhibit mirrored velocity distributions, suggesting a mutual interaction between them. As expected, the amplitude of the acoustic-induced velocity is higher near the resonance frequency.

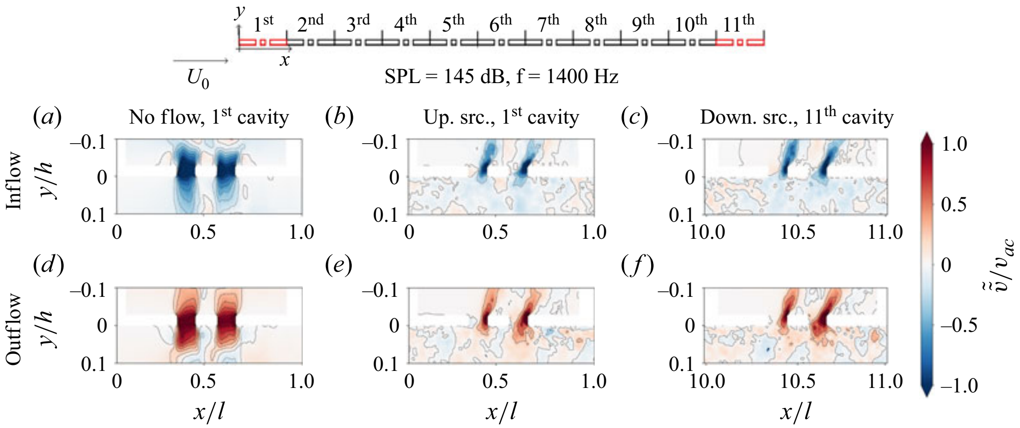

Figure 25. Contour plots of the acoustic-induced velocity inside the orifices for different acoustic source locations relative to the grazing flow. The top row represents the peak of the inflow phase, while the bottom row corresponds to the peak of the outflow phase. Acoustic source: SPL = 145 dB, $f = 1400$ Hz. The phase locking has been performed on the first orifice of each cavity with respect to the acoustic source propagation direction.

When the grazing flow is introduced, the spatial distribution of the acoustic-induced velocity in the orifice changes. The quasi-steady vortex formed on the upstream edge of the orifice opposes the penetration of the acoustic velocity. Therefore, only the downstream half of each orifice is largely subjected to the periodic acoustic-induced motion. The spatial distribution is slightly affected by the frequency of the acoustic wave. Interestingly, for all the frequencies, the amplitude of the maximum velocity is very similar between the no-flow and the grazing flow cases. These observations agree with previous observations that one of the effects of the grazing flow is to reduce the effective porosity of the liner (Zhang & Bodony 2016; Avallone & Casalino 2021). Finally, even though the wavelength exceeds the size of the cavity, there is still a delay in the time at which maximum velocity is reached at the two successive orifices.

By comparing the spatial distributions of the acoustic-induced velocity, it can be noticed that, while for the inflow phase, the acoustic-induced velocity penetrates within the cavity, for the outflow phase, the acoustic-induced velocity weakly penetrates within the turbulent grazing flow, thus suggesting that the flow opposes the ejection of acoustic-induced velocity from the cavity.

As described earlier, the streamwise evolution of the flow modifies the shear layer over the orifices and, therefore, depending on the shear strength and the local SPL, the way the acoustic wave penetrates within the orifice might differ. For this reason, the acoustic-induced velocity fields are shown for the first and last of the cavities in figure 25. The contours of the acoustic-induced flow field are compared for the upstream- and downstream-propagating acoustic waves. Only the case with the acoustic wave amplitude equal to 145 dB and frequency equal to 1400 Hz is shown for the sake of brevity.

The figure highlights the role of the shear layer over the orifices. As a matter of fact, for a given SPL, over the last cavity, the shear-layer strength is lower, as it was shown in figure 19. Consequently, both during the inflow and outflow phases, the high-intensity region of the acoustic-induced velocity is more spread within the orifice. This behaviour is particularly evident when comparing the first and last orifices – i.e. those initially exposed to the acoustic wave. This suggests the streamwise development of the flow over the liner has an impact on how each cavity contributes to the acoustic dissipation.

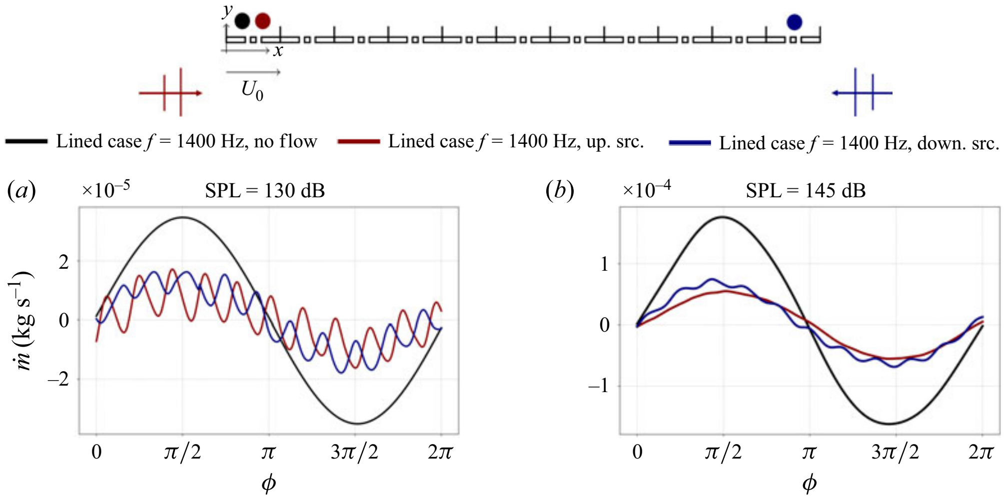

Figure 26. Comparison of the phase-locked mass flow rate over a cycle for a whole cavity; (*a*) SPL = 130 dB, (*b*) SPL = 145 dB.

6.2. *Mass flow rate within the orifices*

To quantify the impact of the flow development, and in particular of the displacement of the near-wall flow over the liner, the phase-averaged mass flow rate $\dot{m}(\phi)$ through each cavity has been calculated as

$$\dot{m}(\phi) = \int_{A_o} \rho(\boldsymbol{x}, \boldsymbol{\phi})\ \tilde{\boldsymbol{v}}(\boldsymbol{x}, \boldsymbol{\phi}) \boldsymbol{\cdot} \boldsymbol{n}\, \mathrm{d}A_o, \tag{6.2}$$

where A_o is the area of the eight orifices. Therefore, the mass flow rate is computed as the integral of the mass flux through the eight orifices of the cavity.

Figure 26(*a*) shows the phase-averaged mass flow rate over one acoustic cycle for plane waves with SPL equal to 130 and 145 dB over the first and last cavities. For the lowest SPL, the mass flow is one order of magnitude lower than at 145 dB. However, for both values of SPLs, the mass flow decreases in the presence of grazing flow, because of the reduction of the effective area due to the quasi-steady vortex. At 130 dB, there is almost no difference between the upstream and downstream cases. Based on the previous findings, this is likely related to the fact that the amplitude of the acoustic source is of the same order as turbulent velocity fluctuations. With SPL = 145 dB, the mass flow rate is higher over the last cavity. The weaker shear layer over the last cavity leads to an increased capability of the acoustic wave to penetrate inside the cavity, as described earlier. The higher-frequency fluctuations visible for both cases in the presence of flow are due to the acoustic fluctuation associated with the cavity depth mode that triggers a shear-layer instability over the orifice, thereby generating a Rossiter-like mode. This feature is identified at both SPLs, and it also persists in the absence of acoustic forcing. This confirms that it is not driven by the external excitation but rather corresponds to an intrinsic aerodynamic mode of the system, influenced by the cavity geometry and orifice shape (Dacome, Siebols & Baars 2024).

Theoretical background on such cavity modes is provided in Panton & Miller (1975), while recent experimental evidence of similar high-frequency tones has been reported by Dacome *et al.* (2024). Moreover, a modal decomposition analysis, performed on a subset of the present dataset (Scarano *et al.* 2025), revealed a mode corresponding to the self-excited tone at 14 kHz.

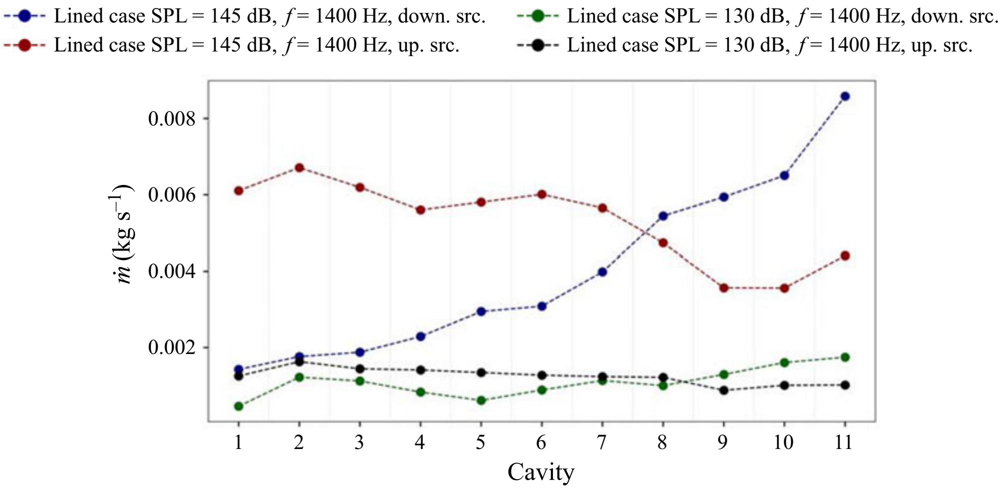

Figure 27. Streamwise evolution of the mass flow rate computed as the integral over the inflow phase.

Figure 27 reports the streamwise distribution of mass flow computed as the integral over the inflow phase (0 to π in figure 26*a*–*b*). It is evident that, for a given SPL, i.e. 145 dB, the mass flow is higher by approximately 22 % at the last cavity for the downstream acoustic source with respect to the first cavity for the upstream acoustic source. This is more evident for the 145 dB case because the amplitude of the acoustic fluctuations is higher; it is less evident for the 130 dB case, but the trend is comparable.

Referring to the SPL decay presented in figure 7, the different slopes between the different acoustic source locations may be explained by the different shear strengths over the orifices along the liner. Therefore, when the acoustic wave propagates in the direction opposite to the mean flow, it first encounters a thicker boundary layer displacement thickness and orifices with weaker shear strength, and then ones with larger shear strength and smaller boundary layer displacement thickness. The opposite happens for the upstream-located acoustic source. This supports the idea that, in conventional facilities, the boundary layer cannot be assumed to be thin. Its development over the liner must be accounted for, as it plays a crucial role in the interaction between the acoustic field and the flow. Furthermore, this finding suggests that the flow development must be considered in eduction methods, which is not the case for the methods currently adopted.

7. Conclusions

Lattice-Boltzmann very-large-eddy simulations of a SDOF locally reacting liner in the presence of grazing flow and grazing acoustic waves were performed. The geometry and turbulent flow conditions replicated experiments carried out in the flow impedance tube at the Federal University of Santa Catarina. Simulations of a single row of 11 cavities were carried out. The impact of the acoustic wave amplitude, frequency and propagation direction was analysed. The resulting database provides a comprehensive benchmark for future modelling, physical interpretation and data-driven analysis of flow–acoustic coupling in these systems. Numerical simulations, validated against experimental measurements of impedance, confirm that the presence of the grazing flow increases the resistance component of impedance and that, when using eduction techniques, differences are present when varying the propagation direction of the acoustic wave with respect to the mean flow.

Numerical simulations were used to compute the local impedance over the entire liner surface using the *in situ* method of Dean. It was found that, using this method, the value of impedance changes largely depending on the sampling location over the face sheet. Furthermore, differences are found when comparing impedance computed using the *in situ* and the MM method, in agreement with experimental findings. Interestingly, although the *in situ* method is sensitive to the sampling location, when impedance is averaged over the surface, it does not depend on the propagation direction of the acoustic wave. On the other hand, this discrepancy is more evident when looking at the results obtained with the MM method. The streamwise distribution of impedance obtained with the *in situ* method suggested that local flow features near the wall play a role by enhancing or reducing the local SPL. This was confirmed by looking at the flow field near the face sheet surface.

The presence of orifices, coupled with the periodic injection of momentum due to the reaction of the liner to the acoustic excitation, causes the displacement of flow further away from the face sheet surface. Therefore, the boundary layer displacement thickness (δ^*), already recognised as a key parameter in semi-empirical models, has been shown to vary significantly along the liner surface. The increase of the boundary layer displacement thickness in the streamwise direction causes the shear layer over downstream orifices to be weaker, thus allowing a larger portion of the orifice to be subjected to the periodic acoustic-induced flow field. This was confirmed by looking at the spatial distribution of acoustic-induced velocity and mass flow rate. The latter increases, for the downstream cavity when the acoustic wave propagates against the turbulent flow. As a consequence of an increase in the effective area and a weaker shear layer, the near-wall field seen by the acoustic wave over the cavities changes if the acoustic wave propagates in the same direction as or opposite to the mean flow. Moreover, the differences in the turbulent flow and the local δ^* lead to distinct shear-flow profiles and velocity fluctuations seen by the acoustic wave depending on their propagation direction, which in turn might modify the portion of the acoustic field that is scattered and refracted at the wall impedance discontinuity.

The findings of this paper suggest that acoustic energy is dissipated differently along the liner because the development of the flow near the wall affects the shear-layer strength over the orifices. This aspect is not accounted for in the boundary conditions adopted for educing impedance and may therefore impact the measured impedance. It is essential to account for the finite boundary layer; in particular, the value of the boundary layer displacement thickness and its growth cannot be neglected. This also suggests that eduction methods based on streamwise varying impedance might be a good choice for a proper characterisation of the acoustic liners.

Future studies shall investigate a longer liner and compare two boundary layer profiles at similar bulk or centreline Mach numbers to evaluate the impact of a higher δ^*/L and different δ^*/d on the acoustic response of the liner.

Supplementary material. Supplementary material is available at https://doi.org/10.1017/jfm.2026.11544.

Acknowledgements. The authors acknowledge the AeroAcoustics Research Consortium (AARC) for supporting pre-competitive research in aircraft noise reduction.

Funding. A.P., F.S. and F.A. were co-funded by the European Research Council (ERC, LINING, grant no. 101075903). The views expressed are those of the authors and do not necessarily reflect those of the European Union or the ERC; neither the European Union nor the granting authority can be held responsible for them. J.A.C. was supported by CNPq (Brazil) under process no. 315000/2021-0.

Declaration of interests. The authors report no conflicts of interest.

Data availability statement. The simulations data are available at https://zenodo.org/records/19565103.

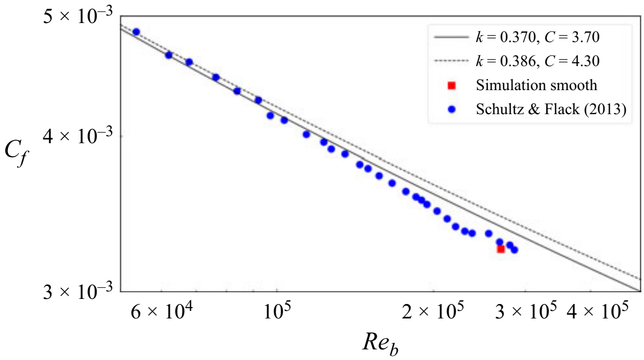

Figure 28. Comparison of skin friction coefficient with friction law (A1) and experiments. The solid line indicates the friction law (A1), while experimental data are by Schultz & Flack (2013).

Appendix A

A.1. *Numerical validation*

The friction coefficient C_f has been computed for the smooth-wall case to validate the simulations. In a channel flow, the friction coefficient is defined as $C_f = 2\tau_w/(\rho u_b^2)$, where $\tau_w = -\mathrm{d}p/\mathrm{d}x \cdot \delta$ and $u_b = \int_0^{2h} u\mathrm{d}y/(2h)$ is the bulk velocity.

In figure 28, the simulation results are shown together with the experimental findings from Schultz & Flack (2013) and the results from Prandtl's smooth-wall flow formula

$$\sqrt{\frac{2}{C_f}} = \frac{1}{k}\log\left(\frac{Re_b}{2}\sqrt{\frac{C_f}{2}}\right) + C - \frac{1}{k}, \tag{A1}$$

where $Re_b = 2hu_b/\nu$ is the Reynolds bulk. Prandtl's formula has been tested with two different sets of log-law coefficients: those suggested by Nagib & Chauhan (2008), $k = 0.370$, $C = 3.70$; and those suggested by Bernardini, Pirozzoli & Orlandi (2014), $k = 0.386$, $C = 4.30$. While the discrepancies are minor for $Re_b < 2\times10^5$, those tend to increase with increasing Re_b. A closer agreement is found between simulation data and Nagib's set of coefficients. Overall, results from the numerical simulations are in line with expectations.

A.2. *Computational cost*

To provide the reader with an indication of the computational effort required to build the present numerical database, an overview of the associated cost is given below. The preliminary flow-convergence simulations, run on 10 computer nodes with 48 processors each, required a total of 341.86 wall-clock hours. To optimise computational resources, coarser simulations were first carried out to develop the flow field within the channel; their solutions were then used to initialise the fine-grid acoustic simulations.

The acoustic simulations were performed on 8 compute nodes (383 solver processes in total) connected via InfiniBand, using single precision and AVX2 vectorisation. Each case contained approximately 1.1×10^9 voxels with 8 refinement levels and was advanced for 3.84×10^5 time steps, requiring 86 hours of wall-clock time and 3.3×10^4 CPU-hours, corresponding to an average performance of 1.25 time steps per second.

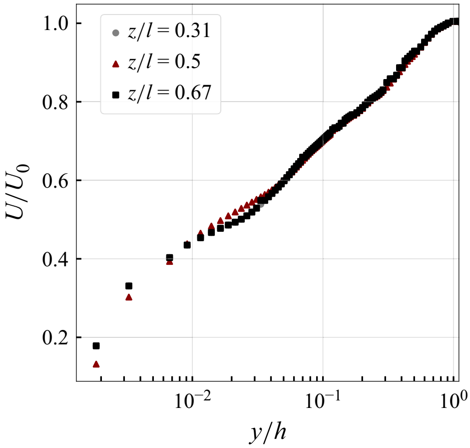

Figure 29. Boundary layer velocity profiles upstream of the liner and at three spanwise locations in the absence of acoustic waves.

Appendix B

The analysis concerning the streamwise evolution of the flow profile and second-order statistics has been conducted on a streamwise plane located at $z/l = 0.5$, i.e. at the mid-span of the channel flow with periodic boundary conditions. Since the orifices do not have the same distribution in the span, figure 29 shows that the velocity profile upstream of the liner is weakly affected by the span. Differences are present in terms of streamwise evolution because of the large number of orifices, but these do not affect the overall conclusions of the paper.

REFERENCES

AURÉGAN, Y., STAROBINSKI, R. & PAGNEUX, V. 2001 Influence of grazing flow and dissipation effects on the acoustic boundary conditions at a lined wall. *J. Acoust. Soc. Am.* **109** (1), 59–64.

AVALLONE, F. & CASALINO, D. 2021 Acoustic-induced velocity in a multi-orifice acoustic liner grazed by a turbulent boundary layer. In *AIAA Aviation and Aeronautics Forum and Exposition, AIAA AVIATION Forum 2021*. American Institute of Aeronautics and Astronautics Inc. AIAA.

AVALLONE, F., MANJUNATH, P., RAGNI, D. & CASALINO, D. 2019 Lattice-Boltzmann very large eddy simulation of a multi-orifice acoustic liner with turbulent grazing flow. In *25th AIAA/CEAS Aeroacoustics Conference, 2019*. American Institute of Aeronautics and Astronautics.

AVALLONE, F., PADUANO, A., PEREIRA, L.M., BONOMO, L.A., CORDIOLI, J.A., CASALINO, D. & CERIZZA, D. 2024 On the comparison of different methods for impedance eduction applied to a numerical database. In *30th AIAA/CEAS Aeroacoustics Conference 2024*.

BAUMEISTER, K.J. & RICE, E.J. 1975 Visual study of the effect of grazing flow on the oscillatory flow in a resonator orifice. *NASA Tech. Memo.* NASA-TM-X-3288, E-8339. NASA Lewis Research Center.

BERNARDINI, M., PIROZZOLI, S. & ORLANDI, P. 2014 Velocity statistics in turbulent channel flow up to $re_{au} = 4000$. *J. Fluid Mech.* **742**, 171–191.

BHATNAGAR, P.L., GROSS, E.P. & KROOK, M. 1954 A model for collision processes in gases. I. Small amplitude processes in charged and neutral one-component systems. *Phys. Rev.* **94** (3), 511–525.

BONOMO, L.A., QUINTINO, N.T., CORDIOLI, J.A., AVALLONE, F., JONES, M.G., HOWERTON, B.M. & NARK, D.M. 2023 A comparison of impedance eduction test rigs with different flow profiles. In *AIAA AVIATION 2023 Forum*. American Institute of Aeronautics and Astronautics.

BONOMO, L.A., QUINTINO, N.T., SPILLERE, A.M.N., CORDIOLI, J.A. & MURRAY, P.B. 2022 A comparison of in-situ and impedance eduction experimental techniques for acoustic liners with grazing flow and high SPL. In *28th AIAA/CEAS Aeroacoustics Conference*. American Institute of Aeronautics and Astronautics.

BRAMBLEY, E.J. 2011 Well-posed boundary condition for acoustic liners in straight ducts with flow. *AIAA J.* **49** (6), 1272–1282.

CASALINO, D., HAZIR, A. & MANN, A. 2018 Turbofan broadband noise prediction using the lattice Boltzmann method. *AIAA J.* **56** (2), 609–628.

CLAUSER, F.H. 1954 Turbulent boundary layers in adverse pressure gradients. *J. Aeronaut. Sci.* **21** (2), 91–108.

CUMMINGS, A. 1976 Sound attenuation in ducts lined on two opposite walls with porous material, with some applications to splitters. *J. Sound Vib.* **49** (1), 9–35.

CUMMINGS, A. 1987 The response of a resonator under a turbulent boundary layer to a high amplitude non-harmonic sound field. *J. Sound Vib.* **115** (2), 321–328.

DACOME, G., SIEBOLS, R. & BAARS, W.J. 2024 Small-scale Helmholtz resonators with grazing turbulent boundary layer flow. *J. Turbul.* **25** (12), 461–481.

DEAN, P.D. 1974 An in situ method of wall acoustic impedance measurement in flow ducts. *Tech. Rep.* 1.

ELNADY, T. & BODÉN, H. 2004 An inverse analytical method for extracting liner impedance from pressure measurements. In *Collection of Technical Papers – 10th AIAA/CEAS Aeroacoustics Conference*, vol. 1. American Institute of Aeronautics and Astronautics.

ELNADY, T., BODÉN, H. & ELHADIDI, B. 2009 Validation of an inverse semi-analytical technique to educe liner impedance. *AIAA J.* **47** (12), 2836–2844.

HERSH, A.S. & WALKER, B. 1979 Effect of grazing flow on the acoustic impedance of Helmholtz resonators consisting of single and clustered orifices. *NASA Contractor Rep.* NASA-CR-3177. NASA Lewis Research Center.

HOWE, M.S. 1984 On the absorption of sound by turbulence and other hydrodynamic flows. *IMA J. Appl. Maths* **32** (1–3), 187–209.

HOWE, M.S. 1996 Emendation of the Brown & Michael equation, with application to sound generation by vortex motion near a half-plane. *J. Fluid Mech.* **329**, 89–101.

HUGHES, C. 2011 The promise and challenges of ultra high bypass ratio engine technology and integration. In *Presentation at the 49th AIAA Aero Sciences Meeting*.

INGARD, U. 1959 Influence of fluid motion past a plane boundary on sound reflection, absorption, and transmission. *J. Acoust. Soc. Am.* **31** (7), 1035–1036.

JAISWAL, P. & GANAPATHISUBRAMANI, B. 2024 Effects of porous substrates on the structure of turbulent boundary layers. *J. Fluid Mech.* **980**, A39.

JIMÉNEZ, J. 2004 Turbulent flows over rough wall. *Annu. Rev. Fluid Mech.* **36**, 173–196.

JONES, M.G., TRACY, M.B., WATSON, W.R. & PARROTT, T.L. 2002 Effects of liner geometry on acoustic impedance. In *8th AIAA/CEAS Aeroacoustics Conference and Exhibit*. American Institute of Aeronautics and Astronautics Inc.

KOOIJMAN, G., HIRSCHBERG, A. & GOLLIARD, J. 2008 Acoustical response of orifices under grazing flow: effect of boundary layer profile and edge geometry. *J. Sound Vib.* **315** (4–5), 849–874.

LAUNDER, B.E. & SPALDING, D.B. 1974 The numerical computation of turbulent flows. *Comput. Meth. Appl. Mech. Engng* **3** (2), 269–289.

LÉON, O., MÉRY, F., PIOT, E. & CONTE, C. 2019 Near-wall aerodynamic response of an acoustic liner to harmonic excitation with grazing flow. *Exp. Fluids* **60** (9), 144.

LEVENBERG, K. 1944 A method for the solution of certain non-linear problems in least squares. *Q. Appl. Maths* **2** (2), 164–168.

MALLAT, S.G. 1989 A theory for multiresolution signal decomposition: the wavelet representation. *Tech. Rep.* 7.

MARQUARDT, D.W. 1963 An algorithm for least-squares estimation of nonlinear parameters. *J. Soc. Ind. Appl. Maths* **11** (2), 431–441.

MELLING, T.H. 1973 The acoustic impedance of perforates at medium and high sound pressure levels. *Tech. Rep.* 1.

MORSE, P.M.C., INGARD, K.U. & MORSE, P.M. 1968 *Theoretical Acoustics: By Philip M. Morse and K. Uno Ingard*. McGraw-Hill.

MOTSINGER, R.E. & KRAFT, R.E. 1991 Design and performance of duct acoustic treatment. In *Aeroacoustics of Flight Vehicles: Theory and Practice. Volume 2: Noise Control* (ed. H.H. Hubbard), chap. 14, pp. 165–206. National Aeronautics and Space Administration.

MURRAY, P.B. & ASTLEY, J.R. 2012 Development of a single degree of freedom perforate impedance model under grazing flow and high SPL. In *18th AIAA/CEAS Aeroacoustics Conference, AIAA Paper* 2012-2294. American Institute of Aeronautics and Astronautics.

MYERS, M.K. 1980 On the acoustic boundary condition in the presence of flow. *J. Sound Vib.* **71** (3), 429–434.

NAGIB, H.M. & CHAUHAN, K.A. 2008 Variations of von Kármán coefficient in canonical flows. *Phys. Fluids* **20**, 101518.

NAYFEH, A.H., KAISER, J.E. & SHAKER, B.S. 1974 Effect of mean-velocity profile shapes on sound transmission through two-dimensional ducts. *J. Sound Vib.* **34** (3), 413–423.

NILSSON, B. & BRANDER, O. 1980 The propagation of sound in cylindrical ducts with mean flow and bulk-reacting lining I. Modes in an infinite duct. *IMA J. Appl. Maths* **26** (3), 269–298.

PADUANO, A., PEREIRA, L.M., BONOMO, L.A., CORDIOLI, J.A., CASALINO, D. & AVALLONE, F. 2024 On the impact of the acoustic wave direction on the in-orifice flow dynamics of an acoustic liner grazed by a turbulent flow. In *30th AIAA/CEAS Aeroacoustics Conference, AIAA Paper* 2024-3122. American Institute of Aeronautics and Astronautics.

PANTON, R.L. & MILLER, J.M. 1975 Resonant frequencies of cylindrical Helmholtz resonators. *J. Acoust. Soc. Am.* **57** (6), 1533–1535.

PEREIRA, L.M., BONOMO, L.A., QUINTINO, N.T., DA SILVA, A.R., CORDIOLI, J.A. & AVALLONE, F. 2023 Validation of high-fidelity numerical simulations of acoustic liners under grazing flow. In *AIAA AVIATION 2023 Forum, AIAA Paper* 2023-3503. American Institute of Aeronautics and Astronautics.

QIAN, Y.H., D'HUMIÈRES, D. & LALLEMAND, P. 1992 Lattice BGK Models for Navier–Stokes Equation. *Europhys. Lett. (EPL)* **17** (6), 479–484.

QUINTINO, N.T., BONOMO, L.A., CORDIOLI, J.A., JONES, M.G., HOWERTON, B.M., NARK, D.M. & AVALLONE, F. 2025 Comparison of impedance eduction test rigs with different boundary-layer profiles. *AIAA J.* **63** (11), 4872–4883.

RENOU, Y. & AURÉGAN, Y. 2011 Failure of the Ingard–Myers boundary condition for a lined duct: an experimental investigation. *J. Acoust. Soc. Am.* **130** (1), 52–60.

RIENSTRA, S.W. & DARAU, M. 2011 Boundary-layer thickness effects of the hydrodynamic instability along an impedance wall. *J. Fluid Mech.* **671**, 559–573.

RIENSTRA, S.W. & HIRSCHBERG, A. 2004 *An Introduction to Acoustic*. Technische Universiteit Eindhoven.

RONCEN, R. 2025*a* Revisiting nonlinear impedance in acoustic liners. *J. Sound Vib.* **608**, 119058.

RONCEN, R. 2025*b* Revisiting nonlinear impedance in acoustic liners. *J. Sound Vib.* **608**, 119058.

SAVERNA, C., AURÉGAN, Y. & PAGNEUX, V. 2019 Non-reciprocal scattering in shear flow. *J. Acoust. Soc. Am.* **146** (2), 1051–1060.

SCARANO, F., JACOB, M.C. & GOWREE, E.R. 2024 Large scale structures modification of a spatially evolving turbulent boundary layer grazing over circular cavities. *Intl J. Heat Fluid Flow* **108**, 109486.

SCARANO, F., LYU, B., PADUANO, A. & AVALLONE, F. 2025 Filtering acoustic from hydrodynamic velocity using modal decomposition methods on an acoustic liner under grazing turbulent flow. *J. Sound Vib.* **625**, 119568.

SCHULTZ, M.P. & FLACK, K.A. 2013 Reynolds-number scaling of turbulent channel flow. *Phys. Fluids* **25**, 025104.

SCHULZ, A., RONNEBERGER, R., WENG, C. & BAKE, F. 2021 The effect of the convective momentum transfer on the acoustic boundary condition of perforated liners with grazing mean flow. *Intl J. Aeroacoust.* **20** (5–7), 737–772.

SCHUSTER, B. 2012 A comparison of ensemble averaging methods using Dean's method for in-situ impedance measurements. In *18th AIAA/CEAS Aeroacoustics Conference, AIAA Paper* 2012-2244. American Institute of Aeronautics and Astronautics.

SHAHZAD, H., HICKEL, S. & MODESTI, D. 2023*a* *Direct Numerical Simulation of a Turbulent Boundary Layer Over Acoustic Liners*. American Institute of Aeronautics and Astronautics (AIAA).

SHAHZAD, H., HICKEL, S. & MODESTI, D. 2023*b* Turbulence and added drag over acoustic liners. *J. Fluid Mech.* **965**, A10.

SPILLERE, A.M.N., BONOMO, L.A., CORDIOLI, J.A. & BRAMBLEY, E.J. 2020 Experimentally testing impedance boundary conditions for acoustic liners with flow: beyond upstream and downstream. *J. Sound Vib.* **489**, 115676.

SUCCI, S. 2001 *The Lattice Boltzmann Equation for Fluid Dynamics and Beyond*. Oxford University Press.

SUTLIFF, D.L. 2021 Liner development at low technology readiness level utilizing the advanced noise control fan. *Intl J. Aeroacoust.*. **20** (5–7), 680–707.

TAM, C.K.W., JU, H., JONES, M.G., WATSON, W.R. & PARROTT, T.L. 2010 A computational and experimental study of resonators in three dimensions. *J. Sound Vib.* **329** (24), 5164–5193.

TAM, C.K.W. & KURBATSKII, K.A. 2000*a* Microfluid dynamics and acoustics of resonant liners. *AIAA J.* **38** (8), 1331–1339.

TAM, C.K.W., PASTOUCHENKO, N.N., JONES, M.G. & WATSON, W.R. 2014 Experimental validation of numerical simulations for an acoustic liner in grazing flow: self-noise and added drag. *J. Sound Vib.* **333**, 2831–2854.

TAM, C.K.W. & KURBATSKII, K.A. 2000*b* Microfluid dynamics and acoustics of resonant liners. *AIAA J.* **38** (8), 1331–1339.

TANG, Y., WANG, P. & LIU, Y. 2024 PIV measurements of coherent vortices and turbulence production inside acoustic liner cavity with offset slit. *Exp. Therm. Fluid Sci.* **154**, 111157.

TEMIZ, M.A., LOPEZ ARTEAGA, I., EFRAIMSSON, G., ÅBOM, M. & HIRSCHBERG, A. 2015 The influence of edge geometry on end-correction coefficients in micro perforated plates. *J. Acoust. Soc. Am.* **138** (6), 3668–3677.

TEXEIRA, C.M. 1998 Incorporating turbulence models into the Lattice-Boltzmann method. *Intl J. Mod. Phys. C* **9** (8), 1159–1175.

VALLIKIVI, M., HULTMARK, M. & SMITS, A.J. 2015 Turbulent boundary layer statistics at very high Reynolds number. *J. Fluid Mech.* **779**, 371–389.

YAKHOT, V. & ORSZAG, S.A. 1986 Renormalization-group analysis of turbulence. *Phys. Rev. Lett.* **57** (14), 1722–1724.

YU, J., RUIZ, M. & KWAN, H.W. 2008 Validation of Goodrich perforate liner impedance model using NASA langley test data. In *14th AIAA/CEAS Aeroacoustics Conference, AIAA Paper* 2008-2930. American Institute of Aeronautics and Astronautics.

ZHANG, Q. & BODONY, D.J. 2012 Numerical investigation and modelling of acoustically excited flow through a circular orifice backed by a hexagonal cavity. *J. Fluid Mech.* **693**, 367–401.

ZHANG, Q. & BODONY, D.J. 2011 Numerical simulation of two-dimensional acoustic liners with high-speed grazing flow. *AIAA J.* **49** (2), 365–382.

ZHANG, Q. & BODONY, D.J. 2016 Numerical investigation of a honeycomb liner grazed by laminar and turbulent boundary layers. *J. Fluid Mech.* **792**, 936–980.